

## Comparison of smart panels for tonal and broadband vibration and sound transmission active control

Paolo Gardonio , Emanuele Turco & Loris Dal Bo

To cite this article: Paolo Gardonio , Emanuele Turco & Loris Dal Bo (2020): Comparison of smart panels for tonal and broadband vibration and sound transmission active control, International Journal of Smart and Nano Materials, DOI: [10.1080/19475411.2020.1825022](https://doi.org/10.1080/19475411.2020.1825022)

To link to this article: <https://doi.org/10.1080/19475411.2020.1825022>



© 2020 The Author(s). Published by Informa UK Limited, trading as Taylor & Francis Group.



Published online: 12 Nov 2020.



Submit your article to this journal [↗](#)



Article views: 112



View related articles [↗](#)



View Crossmark data [↗](#)

## Comparison of smart panels for tonal and broadband vibration and sound transmission active control

Paolo Gardonio, Emanuele Turco and Loris Dal Bo

Dipartimento Politecnico Di Ingegneria E Architettura, Università Degli Studi Di Udine, Udine, Italy

### ABSTRACT

This paper presents a comprehensive overview of the principal features of smart panels equipped with feed-forward and feedback systems for the control of the flexural response and sound transmission due respectively to tonal and to stochastic broadband disturbances. The smart panels are equipped with two types of actuators: first, distributed piezoelectric actuators formed either by small piezoelectric patches or large piezoelectric films bonded on the panels and second, point actuators formed by proof-mass electromagnetic transducers. Also, the panels encompass three types of sensors: first, small capacitive microphone sensors placed in front of the panels; second, distributed piezoelectric sensors formed by large piezoelectric films bonded on the panels and third point sensors formed by miniaturized accelerometers. The proposed systems implement both single-channel and multi-channel feed-forward and feedback control architectures. The study shows that, the vibration and sound radiation control performance of both feed-forward and feedback systems critically depends on the sensor-actuator configurations.

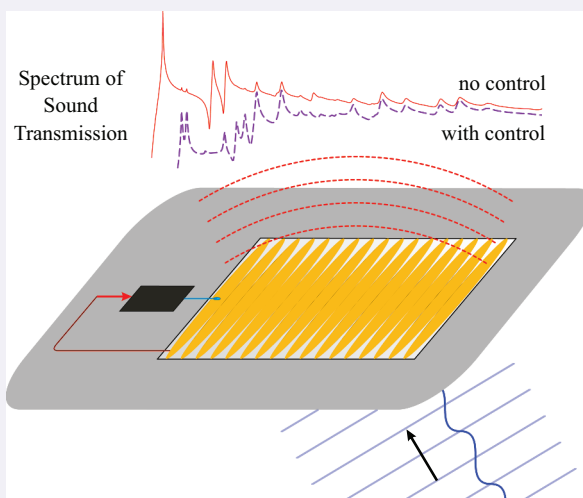
### ARTICLE HISTORY

Received 22 June 2020  
Accepted 14 August 2020

### KEYWORDS

Active structural acoustic control; active vibration control; feed-forward control; feedback control; piezoelectric transducers; proof-mass electromagnetic actuators

Smart Panel for Vibration and Sound Transmission Control



**CONTACT** Paolo Gardonio  [paolo.gardonio@uniud.it](mailto:paolo.gardonio@uniud.it)  Dipartimento Politecnico Ingegneria E Architettura, Università Degli Studi Di Udine, Udine, 33100, Italy

© 2020 The Author(s). Published by Informa UK Limited, trading as Taylor & Francis Group.

This is an Open Access article distributed under the terms of the Creative Commons Attribution-NonCommercial License (<http://creativecommons.org/licenses/by-nc/4.0/>), which permits unrestricted non-commercial use, distribution, and reproduction in any medium, provided the original work is properly cited.

## 1. Introduction

The recent problems of fossil fuel stock decline and climate change have pushed scientist and engineers to explore new designs of fuel-efficient transportation vehicles such as aircrafts, trains, and cars. In this respect, the use of innovative lightweight thin structures has been widely investigated. However, the application of these new structures into the vehicles has posed several new technical challenges, including the abatement of sound transmission to the interior of the vehicles [1–4]. In this respect, over the years, a wide range of materials, designs, treatments, and semi-active and fully active control systems have been investigated and developed to mitigate the vibration and sound transmission of thin walled structures. For instance, quite a vast assortment of innovative composite materials encompassing new micro- and nano-fiber reinforcements or special honeycomb designs have been proposed [5–7]. More recently, new 3D-printed meta-materials characterized by periodic structures based on small-scale unit cells with block masses or resonators have been conceived and built for initial laboratory tests [8,9]. In parallel, several mass, stiffness and damping treatments have been proposed to improve the noise insulation properties of plain thin structures [6,10,11]. Also, double wall constructions encompassing a large variety of porous layers composed by innovative soft fibers or rigid frame porous materials have been introduced in real applications [12,13]. In parallel, passive and semi-active tuneable vibration absorbers (TVAs) have been employed to solve particular problems, such as the control of tonal disturbances or the control of the resonant response of specific flexural modes of thin structures [14,15]. In particular, semi-active TVAs formed by either electromagnetic proof-mass transducers [16,17] or piezoelectric patch transducers [18–20] connected to electrical shunts have been used to develop adaptive TVA systems, which can track the frequency of the tonal excitation or can trace the resonance frequencies of structures subject to significant variations of the working conditions (e.g. tensioning effects, temperature variations, etc.).

During the past two decades, fully active systems were also investigated to control the flexural response and sound transmission of thin structures due to tonal or to stochastic broadband disturbances [6,21]. Historically, the first active noise control systems were formed by multichannel feed-forward controllers encompassing microphone sensors and loudspeaker actuators [22]. However, to guarantee good noise control levels, a rather large number of channels had to be used, which made these systems rather expensive and complex to install and to maintain. Indeed, at each frequency, the acoustic response of an enclosure is given by the overlap of multiple resonant modes, whose number increases proportionally to the cube of frequency [23]. In general, to fully attenuate the sound field of an enclosure, the control system should encompass as many channels as the number of modes forming the acoustic field at the frequency of the disturbance [24]. Therefore, to actively control the interior sound field in vehicles over the typical frequency ranges of the disturbances, the controller should encompass a rather large number of channels. This problem is further aggravated for stochastic noise sources, in which case a rather large number of reference sensors should also be employed to properly reconstruct the primary disturbance. In fact, as shown in Ref. [25], in this case, the control performance is limited to  $1 - \gamma^2$ , where  $\gamma^2$  is the coherence function between the reference signal and the error signal. Therefore, even when the reference signal is strongly correlated to the primary disturbance such that the coherence function is 0.99, the

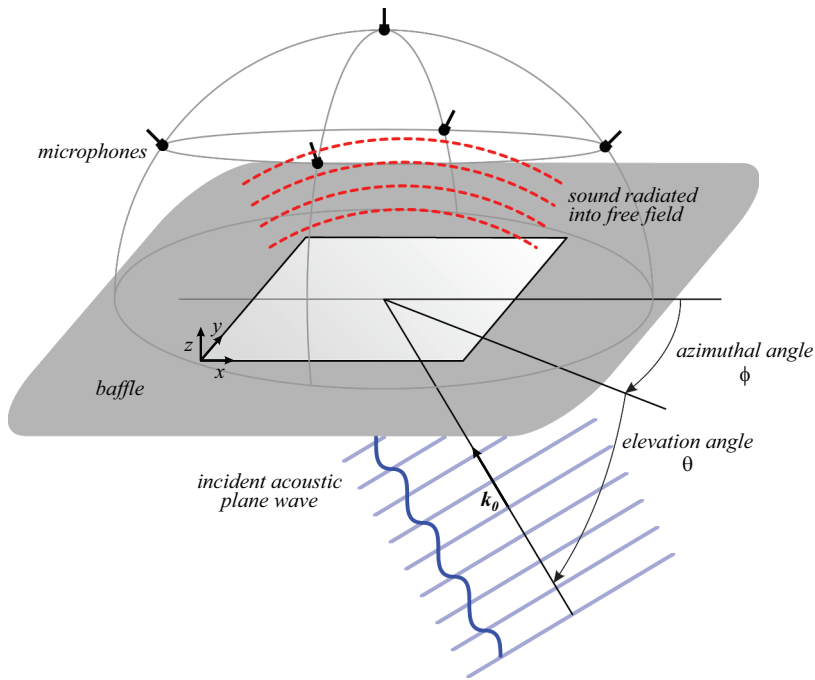
maximum control level that can be achieved is of the order of 20dB. The interior noise in aircraft and cars or trains is normally transmitted via flexural vibrations of the fuselage skin panels or vehicle bodywork panels. The flexural response of thin panels at each frequency is also characterized by the overlap of multiple modes. However, for thin panels, the modal overlap grows linearly with frequency [6,23]. Therefore, for a desired control frequency range, the vibration control system should encompass a smaller number of channels compared to an acoustic control system. Moreover, in this case, the sensors and actuators can be closely located on the panel, so that feedback control architectures can also be employed, which would effectively work on stochastic disturbances [6,25,26]. Therefore, during the past two decades quite a large number of studies have been dedicated to conceive and investigate both feed-forward and feedback vibration control systems, which could be embedded or fixed on thin structures to attenuate either tonal or stochastic sound transmission to the interior of vehicles.

The aim of this paper is thus to present a comprehensive overview of the principal features of smart panels equipped with feed-forward and feedback systems for the control of the flexural response and sound transmission due respectively to tonal disturbances and to stochastic broadband disturbances. This comparative study springs up from a selection of past studies on smart panels for vibration and sound transmission control, which were presented in the following articles [27–32]. The smart panels considered in this study are equipped with two types of actuators: first, distributed piezoelectric actuators formed either by small piezoelectric patches or large piezoelectric films bonded on the panels and second, point actuators formed by proof-mass electromagnetic transducers. Also, the panels encompass three types of sensors: first, small capacitive microphone sensors; second distributed piezoelectric sensors formed by small piezoelectric patches or large piezoelectric films bonded on the panels and, third, point sensors formed by miniaturized accelerometers fabricated with *Micro Systems Technologies* (MST).

The paper is structured in 6 parts. [Section 2](#), introduces the 18 control architectures considered in this paper, where the first 12 are for feed-forward control systems and the remaining 6 are for feedback control systems. [Section 3](#) presents the mathematical model used to derive the flexural response and sound transmission of the thin rectangular smart panels equipped with the feed-forward and the feedback control systems. [Section 4](#) recalls the formulation used to derive the sensing and actuation effects produced by piezoelectric distributed transducers bonded on the thin core panels. [Section 5](#) presents a detailed comparative analysis of the flexural vibration and noise radiation control performances featuring the 18 control systems. Moreover, [section 6](#) shows experimental results obtained with three demonstrators, which were studied in Refs. [33–35]. Finally [Section 7](#) presents a summary of the comparative analysis presented in this paper.

## 2. Smart panels for vibration and sound transmission active control

For simplicity, it is assumed the panels are excited by a plane acoustic wave, which, as shown in [Figure 1](#), impinges the panel with  $45^\circ$  azimuthal and elevation angles. This excitation field couples well with all flexural natural modes of the panel and can be conveniently used to describe the effect of a diffuse acoustic field excitation. As shown in Ref. [32], excitation fields with smaller or larger elevation angles will selectively modify the excitation strength of some low order modes of the panel and produce significant effects



**Figure 1.** Baffled rectangular smart panel excited by a plane acoustic wave and radiating sound into free field.

only at the coincidence frequency, where the sound radiation is maximum. Nevertheless, the coincidence frequency is bound to be greater than the critical frequency [6], which for this panel is of the order of 12 kHz, thus well above the 2 kHz range considered in the study. The panels are baffled and simply supported along the perimeter. They have dimensions  $l_{xp} \times l_{yp} = 278 \times 247\text{mm}$  and the principal material and geometrical properties of the core aluminum panel and piezoelectric transducers are summarized in Table 1.

Tables(2, 3, 4, 5) summarize the smart panels examined in this study. The first 12 panels encompass feed-forward systems for the control of tonal disturbances. More specifically, the first 6 panels shown in Table 2, are characterized by multi-channel feed-forward control systems. For instance, panels (a) and (b) are made by a  $4 \times 4$  array of thin square piezoelectric patch actuators, which are driven by multi-channel feed-forward controllers set to minimize respectively the total noise radiation and the global flexural response of the panel. As shown in the sketches, in practice, the total radiated noise is estimated with an array of 5 microphones whereas the global flexural response of the panel is measured by 16 MST accelerometers located at the centers of the piezoelectric patches. As shown in Figure 1, the 5 microphones are located on hemisphere of radius 1m, which is centered on the middle of the panel. The radius of one microphone is thus oriented normal to the panel and the radii of the other four microphones are oriented along the principal axis of the panel with an elevation angle of  $45^\circ$ . Panels (c) and (d) are also characterized by multi-channel feed-forward controllers. However, in this case the 16 piezoelectric patch actuators have triangular shape and are evenly distributed along the perimeter of the panel with the base edge aligned with the border of the panel. As with the first two panels, the

**Table 1.** Physical properties of the core aluminum panel and PZT and PVDF transducers [38,39,127].

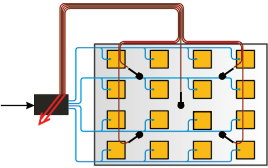
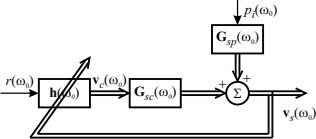
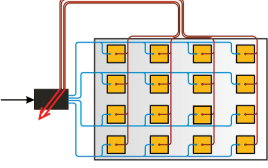
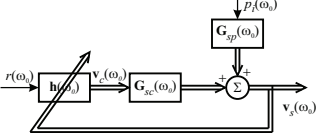
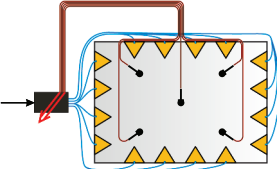
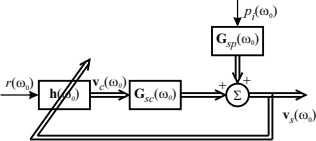
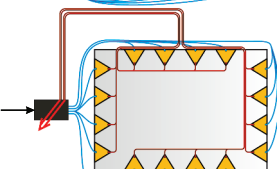
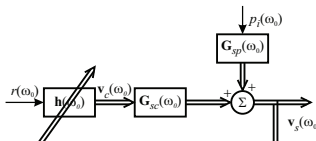
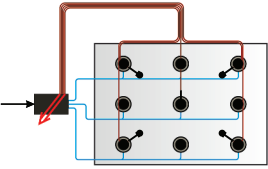
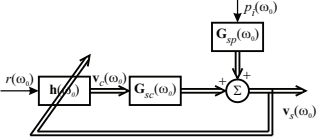
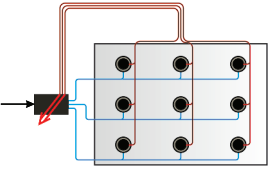
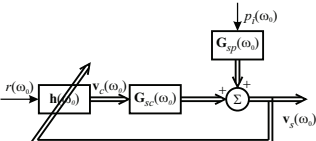
Parameter	Symbol	Aluminum	PZT	PVDF
Density	$\rho_s, \rho_{pe}$	2720 kg/m <sup>3</sup>	7600 kg/m <sup>3</sup>	1780 kg/m <sup>3</sup>
Young's modulus	$E_s, E_{pe}$	$7 \times 10^{10}$ N/m <sup>2</sup>	$6.3 \times 10^{10}$ N/m <sup>2</sup>	$2 \times 10^9$ N/m <sup>2</sup>
Poisson ratio	$\nu_s, \nu_{pe}$	0.33	0.31	0.29
Strain/charge constants	$d_{31}^0$		$166 \times 10^{-12}$ m/V	$23 \times 10^{-12}$ m/V
	$d_{32}^0$		$166 \times 10^{-12}$ m/V	$3 \times 10^{-12}$ m/V
	$d_{36}^0$		0m/V	0m/V

two multichannel controllers are set to minimize respectively the total noise radiation measured by the array of 5 microphones and the global flexural response of the panel, which, in this case, is measured by 16 MST accelerometers located at tips of the triangles. These two arrangements are therefore located along the borders of the panel to form a compact system, which can be conveniently used for windscreens, windows, etc. At last, panels (e) and (f) encompass a  $3 \times 3$  array of small scale proof-mass electromagnetic actuators [36], which are characterized by a very low resonance frequency for the axial oscillations of the elastically suspended proof-mass so that, they generate transverse point forces over the whole frequency range of control [37]. Once more, the two multichannel controllers are set to minimize respectively the total noise radiation measured by the array of 5 microphones and the global flexural response of the panel, which, here, is measured by 9 MST accelerometers located at the footprints of the actuators.

The next 6 panels shown in Table 3, are instead characterized by single-channels feed-forward control systems. To start with, panels (g) and (h) encompass the same  $4 \times 4$  array of thin square piezoelectric patch actuators of panels (a) and (b). However, in this case the 16 patches are driven by a single channel feed-forward controller, which, for panel (g) is set to minimize the total noise radiation measured by the array of 5 microphones and for panel (h) is set to minimize the global flexural vibration of the panel measured by the 16 MST accelerometers located at the centers of the piezoelectric patches. Alternatively, panels (i) and (j) encompass a single piezoelectric film actuator, which covers the whole surface of the panel. The electrodes of the piezoelectric film are characterized by an array of quadratically shaded leafs. As will be discussed in Section 4.3.3, for each leaf, the transducer produces a line bending excitation, so that, in first approximation, the panel is uniformly excited in bending. In panel (i), the single channel feed-forward controller is set to minimize the total noise radiation measured by the array of 5 microphones. Alternatively, in panel (j), the controller is set to minimize the global flexural response of the panel, which, in this case, is measured by a matched piezoelectric film transducer with the quadratically shaded electrodes bonded on the opposite side of the panel. Finally, panels (k) and (l) incorporate the same  $3 \times 3$  array of small-scale proof-mass electromagnetic actuators of panels (e) and (f). However, in this case the 9 actuators are driven by a single channel feed-forward controller, which, for panel (k) is set to minimize the total noise radiation measured by the array of 5 microphones and for panel (l) is set to minimize the global flexural vibration of the panel measured by the 9 MST accelerometers located at the footprints of the actuators.

The final group of 6 panels implement instead feedback control systems. The design of feedback controllers is somewhat more involved, particularly for multi-channel

**Table 2.** Smart panels with multiple-channels feed-forward control systems

TYPE	SKETCH	SCHEME
(a)		
(b)		
(c)		
(d)		
(e)		
(f)		

controllers, and requires reliable models of the dynamic response of the structure [38,39]. This is quite a severe requirement, particularly in view of the fact that the flexural response of thin panels used in transportation vehicles is susceptible to significant variations due to the operation conditions (e.g. tensioning effects, temperature changes, etc.). For this reason, the studies on smart panels with feedback systems for flexural vibration control have been directed toward simpler control architectures. In this paper, two arrangements are considered. The first is exemplified by panels (m), (n), and (o), which, as shown in Table 4, implement decentralized velocity feedback loops [40–43]. More specifically, panel (m) is characterized by a regular  $4 \times 4$  array of velocity feedback loops, each composed by a square piezoelectric patch actuator with a miniaturized MST accelerometer sensor at its


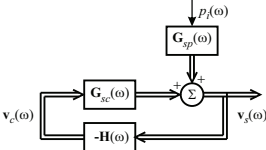
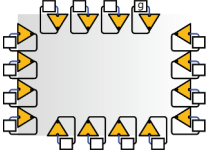
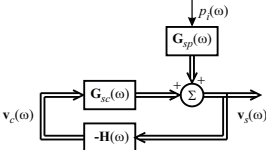
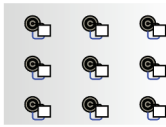
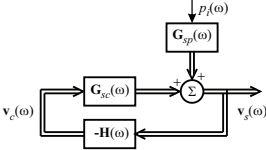
**Table 3.** Smart panels with single-channel feed-forward control systems.

TYPE	SKETCH	SCHEME
(g)		
(h)		
(i)		
(j)		
(k)		
(l)		

center [29,33,40]. As discussed in Refs. [34,44,45], the stability of the overall system can be studied with a similar approach than that of a single channel feedback loop, which is based on a generalized Nyquist criterion [46,47]. This is quite an important feature, since, in first instance, the design of the feedback loops can be redirected to the design of a single velocity feedback loop with the closely located piezoelectric patch and accelerometer sensor pair [37,44,45,48]. Panel (n) is also characterized by an array of 16 decentralized feedback loops, which are arranged along the perimeter of the panel [29]. Each loop is formed by a triangular piezoelectric patch, with the base edge aligned to the border of the panel, and a miniaturized MST accelerometer at the tip. As will be discussed in Section 4.3.2, the triangular piezoelectric actuators produce a transverse force at their



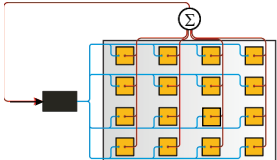
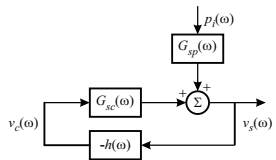
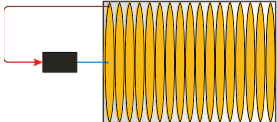
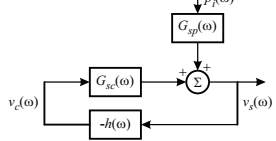
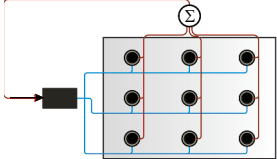
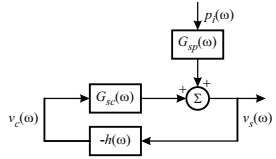
**Table 4.** Smart panels with multiple-channels decentralized feedback control systems.

TYPE	SKETCH	SCHEME
(m)		
(n)		
(o)		

vertices, which is thus dual and collocated with the point velocity measured via the accelerometer. This is quite an interesting feature, particularly in view of the stability of the feedback loop [35]. Finally, panel (o) encompasses a  $3 \times 3$  array of velocity feedback loops, which are formed by proof-mass electromagnetic actuators with a miniaturized MST accelerometer at their footprint. Also in this case, the stability of the feedback loops is enhanced by the fact that the sensor-actuator pairs are collocated. Nevertheless, as discussed in Refs. [30,34,37], the low frequency dynamics of the proof-mass electromagnetic actuator tends to destabilize the feedback loops when too large gains are implemented. Over the years, several solutions have been proposed to solve this problem. For example, the application of relative displacement, relative velocity and force feedback loops between the magnet and armature-coil components were investigated [35,49–52]. Also, the implementation of a compensator in the controller, which moves to a lower value the fundamental resonance frequency of the actuator was proposed [53]. In parallel, the implementation of a non-linear control system to limit the stroke of the proof-mass was studied [54,55]. Finally, the adoption of actuators with a flywheel element have been tested [56,57].

To conclude, the panels (p), (q), and (r) shown in Table 5 are formed by single-channel feedback systems. To start with, panel (p) is formed by the  $4 \times 4$  regular array of square piezoelectric patches with MST accelerometers at their centers. In this case, the 16 patches are driven by the same control signal and the error signal is given by the sum of the signals measured by the 16 accelerometers. Panel (q) is built with the same matched piezoelectric films of panels (i) and (j), which are characterized by an array of quadratically shaded electrodes. Therefore, the system implements a very simple velocity loop where the volume velocity of the panel measured by one piezoelectric film is fed back to the piezoelectric film glued on the opposite face, which, approximately, generates a uniform

**Table 5.** Smart panels with multiple-channels feedback control systems

TYPE	SKETCH	SCHEME
(p)		
(q)		
(r)		

force over the surface of the panel [58]. As will be discussed below, this is quite an appealing simple solution, where the matched volume velocity sensor and uniform force actuator effectively couple with the vibration component of the panel mainly contributing to the sound radiation. Nevertheless, as discussed in Ref. [27], the effectiveness of this setup is greatly influenced by the stability of the feedback loop, which is limited by the fact that the two transducers couple both via out-of-plane flexural vibrations and in-plane extensional and shear vibrations. The two coupling effects are out of phase and thus, although the two transducers are collocated and matched, they are not dual and cannot guarantee unconditional stability properties [27]. In general, the coupling via flexural vibrations dominates at low frequencies, particularly for thick panels. Thus, this sensor-actuator pair can be effectively used on thick honeycomb panels, provided a low-pass filter is implemented in the loop. An alternative solution to this setup is given by panel (r), which, as for panels (k) and (l), is equipped with a  $3 \times 3$  array of proof-mass actuators driven by the same control signal and a matched  $3 \times 3$  array of miniaturized MST accelerometers whose output signals are summed into a single feedback control signal. This setup is quite effective in measuring the volumetric transverse vibration of the panel and in generating a uniform transverse force over the panel. Nevertheless, also in this case, since both the sensing and actuation are not uniformly distributed, the feedback loop cannot guarantee unconditional stability. Therefore, once more, the effectiveness of the control system could be impaired by a low limit of the maximum stable feedback gain that can be implemented.

According to the literature, the control action produced by these smart panels can be classified in two groups: the so-called Active Structural Acoustic Control (ASAC) systems and the so-called Active Vibration Control (AVC) systems. The ASAC systems are made by arrangements where the structural actuators fixed on the panel are driven to minimize its

sound radiation estimated either by microphone acoustic sensors placed in the interior volume or by piezoelectric distributed transducer or accelerometer structural sensors fixed on the panel itself [6,21,38,58–70]. Since the first inception of this idea, quite a vast range of designs have been investigated by scientists, which encompass either distributed strain sensors or arrays of point sensors [71–81] specifically designed to detect the vibration components of a panel that mostly contribute to the far field sound radiation. Also, a considerable amount of efforts has been dedicated to the development of strain actuators in such a way as to have compact and lightweight composite smart structures [73,74,82–90]. The AVC systems are instead characterized by arrangements where the structural actuators mounted on the panel are driven to minimize its vibration field estimated by piezoelectric distributed transducers or accelerometers structural sensors fixed on the panel [6,28–42,45]. As will be shown in the paper, the ASAC approach is particularly suited to control the sound transmission through partitions, although it requires an accurate estimate of the sound radiation, which is not an easy task to attain. The AVC control systems are somewhat more simple system to implement, although they require a careful design to avoid that, as will be shown in the paper, the sound transmission is actually increased.

### 3. Mathematical formulation

The smart panels with feed-forward (panels a–l) and feedback (panels m–r) [6,21,25,38] control systems considered in this study are made either with distributed or point sensor and actuator transducers fixed on a core aluminum panel. The distributed transducers encompass dense arrays of small piezoelectric patch actuators or large piezoelectric film actuators and sensors, which are comparatively thinner than the core panel and cover a substantial portion of the core panel. Moreover, the point sensors and point actuators are formed by extensive arrays of miniaturized MST accelerometers and extensive arrays small-scale proof-mass electromagnetic transducers respectively. Therefore, the mathematical formulation developed to study the flexural vibration and sound transmission control effects produced by the smart panels assumes the sensor and actuator transducers produce uniform stiffening and uniform inertia passive effects smeared over the entire surface of the core panel. Also, the distributed sensing and actuation effects of the piezoelectric transducers are modeled in terms of distributed linear-angular velocities and force-moment excitations. Since the study is focused on the analysis of the flexural response and sound transmission of the smart panels, only the effects produced by the out-of-plane vibrations is considered in the model. However, it should be emphasized that, the coupling between distributed transducers is heavily affected by the in-plane vibrations too, and thus, to accurately study the stability of the control systems, the models should encompass also the effects of in-plane extensional and shear vibrations [27]. The formulation assumes time-harmonic functions, which are given in the following complex form  $f(t) = \text{Re}\{f(\omega)\exp(j\omega t)\}$ , where  $f(\omega)$  is the frequency-dependent complex amplitude,  $\omega$  is the circular frequency and  $j = \sqrt{-1}$ .

### 3.1 Flexural vibration and sound transmission

The flexural response and the sound transmission of the panels are described with respect to the time-averaged total flexural kinetic energy  $E(\omega)$  and time-averaged total radiated sound power  $P(\omega)$ , which for brevity, will be referred to as ‘flexural kinetic energy’ and ‘radiated sound power’. The flexural kinetic energy is used to describe both the flexural response of the panel and the near-field sound radiated by the panel [6]. Instead, the radiated sound power provides information on the far-field sound radiation. Following the formulation presented in Refs. [6,29,31], the flexural kinetic energy and radiated sound power are derived with the following modal expressions:

$$E(\omega) = \frac{\rho_p h_p}{4} \int_0^{l_{xp}} \int_0^{l_{yp}} |\dot{w}(x, y, \omega)|^2 dx dy = \frac{1}{4} m_p \mathbf{a}^H(\omega) \mathbf{a}(\omega) \quad (1)$$

$$P(\omega) = \frac{1}{2} \int_0^{l_{xp}} \int_0^{l_{yp}} \text{Re}\{\dot{w}^*(x, y, \omega) p_0(x, y, \omega)\} dx dy = \mathbf{a}^H(\omega) \mathbf{A}(\omega) \mathbf{a}(\omega) \quad (2)$$

Here,  $m_p = \rho_p h_p l_{xp} l_{yp}$  and  $\rho_p$  are the total mass and the equivalent density of the smart panels. Also  $\dot{w}(x, y, \omega)$  and  $p_0(x, y, \omega)$  are the complex transverse velocity and sound pressure at a generic position  $(x, y)$  on the panel. Finally,  $\mathbf{a}(\omega)$  is a  $N \times 1$  vector with the first  $N$  complex modal velocity amplitudes of the panel flexural vibration. To model accurately the flexural vibration of the panels up to 2 kHz, the contribution of all flexural modes of the simply supported panel with natural frequencies up to 20 kHz have been considered. Such a large number of modes is necessary to properly reconstruct the coupling of the distributed sensors and of the distributed actuators with the flexural vibration fields of the panel. Finally, according to the formulation presented in [6],  $\mathbf{A}(\omega)$  is the  $N \times N$  ‘power transfer matrix’, which for a flat panel is given by

$$\mathbf{A}(\omega) = \frac{\omega \rho_0}{4\pi} \int_0^{l_{xp}} \int_0^{l_{yp}} \int_0^{l_{xp}} \int_0^{l_{yp}} \boldsymbol{\phi}^T(x, y) \frac{\sin(k_0 d)}{d} \boldsymbol{\phi}(x', y') dx' dy' dx dy \quad (3)$$

Here  $k_0 = \omega/c_0$  and  $c_0 = 343 \text{ m/s}$  are respectively the acoustic wavenumber and speed of sound in air,  $\rho_0$  is the density of air,  $d$  is the distance between points  $(x, y)$  and  $(x', y')$  of the panel. Also,  $\boldsymbol{\phi}(x, y)$  is the  $1 \times N$  vector with the first  $N$  flexural natural modes at point  $(x, y)$  of the panel.

The first row in Figure 2 shows the first five flexural modes of the simply supported panel considered in this study. According to Eq. (2) the radiated sound power by the panels is characterized by both the self-radiation effects of the structural modes, which depend on the diagonal terms of the matrix  $\mathbf{A}(\omega)$ , and mutual-radiation effects of pairs of modes, which depend on the off-diagonal terms of the matrix  $\mathbf{A}(\omega)$  [6,71,72]. Figure 3 shows both the diagonal (red lines in Plots a,c) and off-diagonal (black lines in Plots b,d) elements of the matrix  $\mathbf{A}(\omega)$  with reference to the ratio  $k_0/k_b$  between the acoustic and flexural wave numbers. The red lines in Plots (a,c) indicate that all flexural modes effectively radiate sound above the critical frequency  $\omega_c$  such that  $k_0 > k_b$ . At frequencies below  $\omega_c$ , such that  $k_0 < k_b$ , the efficiency tends to fall to 0 as  $\omega \rightarrow 0$ . In general, the natural modes with both odd mode orders are better sound radiators than modes with respectively one or both even mode orders. Therefore, at frequencies below the critical frequency the sound radiation is controlled by the so-called volumetric modes, that is those modes

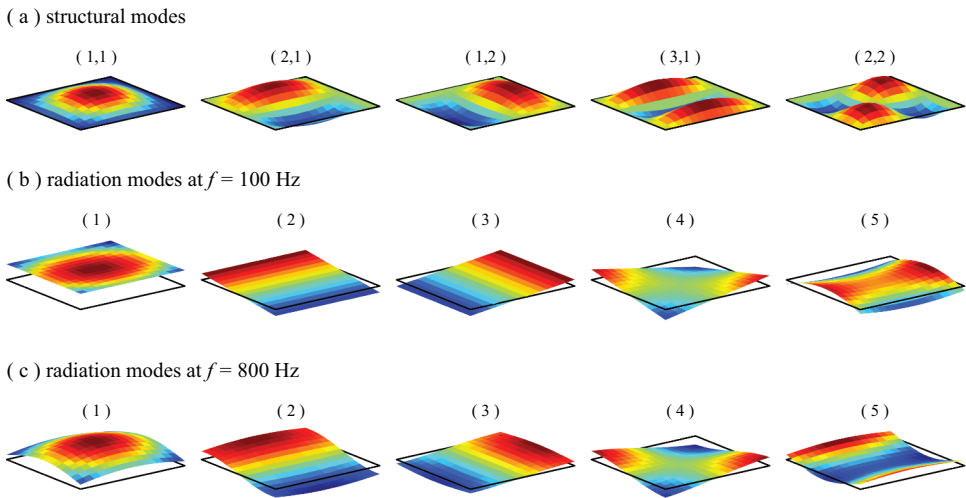


Figure 2. Panel flexural modes (a) and sound radiation modes at 100 Hz (b) and 800 Hz (c).

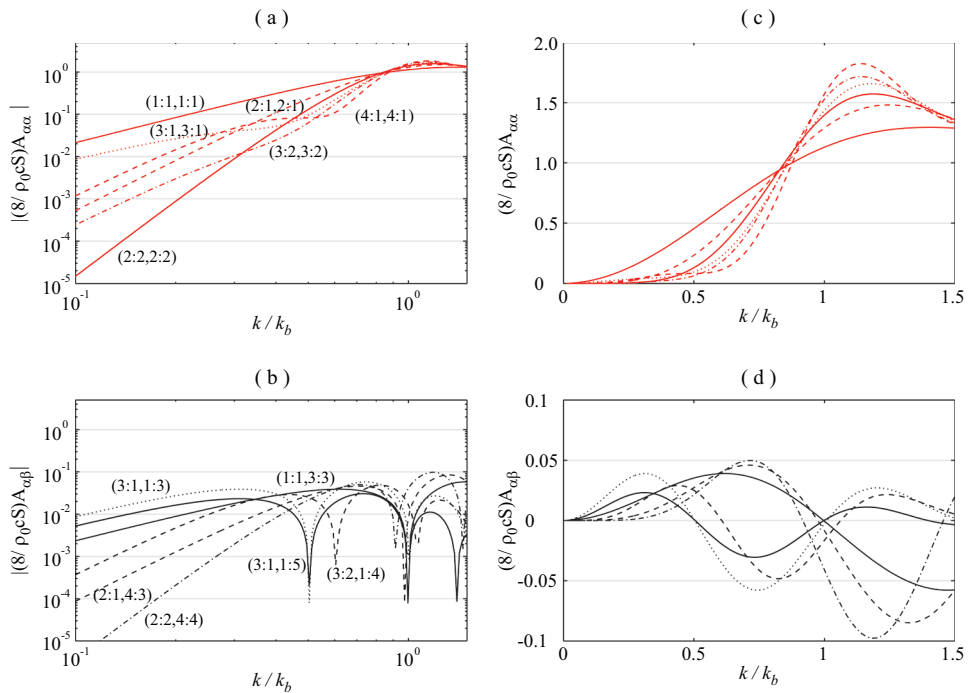
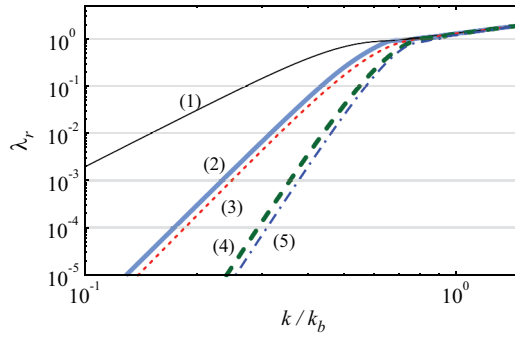


Figure 3. Self (a,c) and mutual (b,d) radiation efficiencies of the rectangular panel plotted in logarithmic (a,b) and linear (c,d) scales.

characterized by a net displacement over the whole surface of the panel. In contrast, above the critical frequency  $\omega_c$ , all modes efficiently contribute to the sound radiation. The black lines shown in Plots (b,d) indicate that the mutual-radiation efficiencies are much smaller than the self-radiation efficiencies. Moreover, they assume both



**Figure 4.** Radiation modes efficiencies.

positive and negative values, such that, the black lines in Plot (b) are characterized by the sharp troughs at those frequencies where the efficiencies approach 0 and then switch sign. Therefore, as discussed in Chapter 3.6 of reference [6], the mutual sound radiation effects produced by pair of modes will either enhance or attenuate the sound radiation within given frequency bands. This suggests that, controlling the vibration field produced by a specific flexural mode of the panel could actually bring to an increment of the sound radiation at those frequency bands where the mutual sound radiation effects of this mode with other modes of the panel would significantly attenuate the sound radiation [21].

The self and mutual-radiation mechanisms described above arise from the shapes of the flexural natural modes. The studies summarized in Refs. [68,91–95] proposed that the sound radiation can also be formulated with respect to a new set of modal functions, which radiate sound independently. As shown in Ref. [6], Since the power transfer matrix  $\mathbf{A}(\omega)$  is normal, that is, it is real, symmetric and positive definite, it is possible to implement the following eigenvalue-eigenvector decomposition

$$\mathbf{A}(\omega) = \mathbf{P}^T(\omega) \mathbf{\Omega}(\omega) \mathbf{P}(\omega) \quad (4)$$

where  $\mathbf{P}(\omega)$  is the  $M \times N$  orthogonal matrix of eigenvectors and  $\mathbf{\Omega}(\omega)$  is the  $M \times M$  diagonal matrix with real and positive eigenvalues. Therefore, the expression given in Eq. (2) for the radiated sound power becomes

$$P(\omega) = \mathbf{b}^H(\omega) \mathbf{\Omega}(\omega) \mathbf{b}(\omega) \quad (5)$$

Here

$$\mathbf{b}(\omega) = \mathbf{P}(\omega) \mathbf{a}(\omega) \quad (6)$$

is a  $M \times 1$  vector of transformed modal amplitudes, which radiate sound independently from each other. These complex modal amplitudes arise from a new set of modes of the panel, which are called 'radiation modes' and are given by the linear combination of the panel flexural modes weighted by the eigenvectors such that, for example, the  $j$ -th radiation mode is given by

$$\psi_j(x, y, \omega) = \phi(x, y) \mathbf{P}_j^T(\omega) \quad (7)$$

where  $\mathbf{P}_j(\omega)$  is the  $j$ -th row of the matrix  $\mathbf{P}(\omega)$ . This expression indicates that, unlike the structural modes, the shapes of the radiation modes depend on frequency. In this case, the radiation efficiencies are given by the eigenvalues in the matrix  $\mathbf{\Omega}(\omega)$ , which are also called ‘radiation modes efficiencies’. The radiation modes efficiencies are normally sorted in descending order. For instance, [Figure 4](#) shows the spectra of the radiation efficiencies for the first five radiation modes with respect to the ratio  $k_o/k_b$ . Also, the second and third rows of [Figure 2](#) show the shapes of the first five radiation modes calculated at 100 Hz and 800 Hz, which can be contrasted with the shapes of the first five structural modes of the panel shown in the first row. [Figure 4](#) shows that, also in this case, all radiation modes effectively radiate sound above the critical frequency  $\omega_c$  such that  $k_o > k_b$ , whereas, at frequencies below  $\omega_c$ , such that  $k_o < k_b$ , the efficiencies tend to fall to 0 as  $\omega \rightarrow 0$ . According to [Figure 2\(b,c\)](#) and 4, the first, and most efficient, radiation mode is characterized by an even transverse displacement of the panel, which tends to be rounded off at higher frequencies. This mode is normally called volumetric mode since it produces a net volumetric displacement of the air. The second and third radiation modes are instead characterized by rocking displacements of the panel, which therefore are less efficient sound radiators. The fourth and fifth modes are characterized by twisting and bending shapes, whose sound radiation efficiency is even lower.

For air, the fluid loading on the panel can be neglected [6], such that the vector with the modal complex velocities for the flexural response of the panel can be expressed in terms of the primary and the  $R$  control excitations as follows [6,28,31]:

$$\mathbf{a}(\omega) = \mathbf{a}_p(\omega)p_i(\omega) + \mathbf{A}_c(\omega)\mathbf{v}_c(\omega) \quad (8)$$

where  $\mathbf{a}_p(\omega)$  is the  $N \times 1$  column vector with the modal complex velocities per unit primary acoustic wave excitation and  $\mathbf{A}_c(\omega)$  is the  $N \times R$  matrix with the modal complex velocities per unit control sources, whose elements are given respectively by [96]:

$$a_p^n(\omega) = \frac{j\omega F_p^n(\omega)}{m_p(\omega_n^2 - \omega^2 + j2\zeta_n\omega\omega_n)} \quad (9)$$

$$A_c^{n,r}(\omega) = \frac{j\omega F_c^{n,r}(\omega)}{m_p(\omega_n^2 - \omega^2 + j2\zeta_n\omega\omega_n)} \quad (10)$$

Here  $\zeta_n$  is the modal damping ratio, which was taken to be 0.01 for all modes in these simulations. Also, assuming the panels are simply supported along the four edges,  $\omega_n =$

$\sqrt{\frac{D_p}{\rho_p h_p} \left[ \left( \frac{n_1\pi}{l_{xp}} \right)^2 + \left( \frac{n_2\pi}{l_{yp}} \right)^2 \right]}$  is the  $n$ -th flexural natural frequency

and  $\varphi_n(x, y) = 2 \sin\left(\frac{n_1\pi x}{l_{xp}}\right) \sin\left(\frac{n_2\pi y}{l_{yp}}\right)$  is the  $n$ -th flexural natural mode, which is characterized by indices  $n_1$  and  $n_2$ . For example, the first five flexural modes of the panels considered in this study are shown in [Figure 2\(a\)](#). In these expressions,  $D_p = \frac{E_p h_p^3}{12(1-\nu_p^2)}$  is

the smeared bending stiffness of the smart panel, which is thus characterized by the equivalent Young’s modulus of elasticity  $E_p$  and the equivalent Poisson ratio  $\nu_p$ . Lastly  $F_p^n(\omega)$  and  $F_c^{n,r}(\omega)$  are the modal excitation terms, which are due respectively to primary sound pressure field generated on the surface of the panel by the impinging plane wave

and to the secondary flexural excitation(s) generated by the control actuator(s) fixed on the panel. The first term, is given by the integral of the sound pressure field generated over the panels surface [97], which for a plane harmonic acoustic wave incident with azimuthal and elevation angles of  $\varphi = 45^\circ$  and  $\theta = 45^\circ$ , is given by:

$$p_i(x, y, t) = \text{Re} \left\{ p_i(\omega) e^{j(\omega t - k_x x - k_y y)} \right\} \quad (11)$$

Here  $p_i(\omega)$  is the complex amplitude of the plane wave, which has a wave numbers in  $x$  and  $y$  directions given by  $k_x = k_0 \sin(\theta) \cos(\varphi)$  and  $k_y = k_0 \sin(\theta) \sin(\varphi)$ . Therefore the modal excitation terms  $F_p^n(\omega)$  due to the primary incoming acoustic wave are given by [96]:

$$F_p^n(\omega) = 2p_i(\omega) \int_0^{l_{xp}} \int_0^{l_{yp}} \varphi_n(x, y) e^{-j(k_x x + k_y y)} dx dy = 2 p_i(\omega) l_{n1} l_{n2} l_{xp} l_{yp} \quad (12)$$

When  $n_1 \pi \neq \pm \alpha_x \sin \theta \cos \varphi$  and  $n_2 \pi \neq \pm \alpha_y \sin \theta \sin \varphi$ , the two coefficients  $l_{n1}$  and  $l_{n2}$  are given by [97]

$$l_{n1} = \frac{n_1 \pi [1 - (-1)^{n_1} \exp(-j \alpha_x \sin \theta \cos \varphi)]}{[n_1 \pi]^2 - [\alpha_x \sin \theta \cos \varphi]^2}, \quad l_{n2} = \frac{n_2 \pi [1 - (-1)^{n_2} \exp(-j \alpha_y \sin \theta \sin \varphi)]}{[n_2 \pi]^2 - [\alpha_y \sin \theta \sin \varphi]^2}. \quad (13a, b)$$

Alternatively, when  $n_1 \pi = \pm \alpha_x \sin \theta \cos \varphi$  and  $n_2 \pi = \pm \alpha_y \sin \theta \sin \varphi$ , they are given by

$$l_{n1} = -\frac{1}{2} j \text{sgn}(\sin \theta \cos \varphi), \quad l_{n2} = -\frac{1}{2} j \text{sgn}(\sin \theta \sin \varphi). \quad (13 c, d)$$

Here  $\text{sgn}()$  is the sign function and  $\alpha_x = \frac{\omega l_{xp}}{c_0}$  and  $\alpha_y = \frac{\omega l_{yp}}{c_0}$ , where  $l_{xp}$ ,  $l_{yp}$  are the dimensions of the plate and  $c_0$  is the speed of sound in air. Similarly, the secondary modal excitation terms  $F_c^{n,r}(\omega)$  too can be derived from an integration over the surface of the panel, in this case, with respect of the excitation field(s) produced by the control actuator(s) on the surface of panels. Therefore, for the proof-mass electromagnetic point actuators, they are simply given by the amplitudes of the panel modes at the control positions. Instead, for the distributed piezoelectric actuators shown in Table 2–5, they are given by somewhat more involved expressions, which are described in details in the following Section 3. To conclude,  $\mathbf{v}_c(\omega)$  is the  $R \times 1$  vector with the complex input voltage signals,  $v_{cr}(\omega)$ , to the  $R$  control piezoelectric transducers.

In this study, the sound transmission through the smart panels is assessed with respect to the sound transmission ratio [6,68,98], which gives the ratio between the time-averaged total radiated sound power and the time-averaged total incident sound power:

$$T(\omega) = \frac{P_r(\omega)}{P_i(\omega)} \quad (14)$$

The time-averaged total incident sound power produced by the plane acoustic wave is given by [68]:

$$P_i(\omega) = \frac{1}{2} \frac{1}{\rho_0 c_0} |p_i(\omega)|^2 l_{xp} l_{yp} \cos(\theta) \quad (15)$$

The vector with the complex control signals,  $v_{ss}(\omega)$ , from the  $S$  control sensors can also be expressed with the following matrix expression:



$$\mathbf{v}_s(\omega) = \mathbf{G}_{sp}(\omega) p_i(\omega) + \mathbf{G}_{sc}(\omega) \mathbf{v}_c(\omega). \quad (16)$$

Here  $\mathbf{v}_s(\omega)$  is the  $S \times 1$  vector with the complex output signals  $v_{ss}(\omega)$  from the  $S$  control sensors, which, according to Table 2–5, are either point accelerometers or distributed piezoelectric transducers. The matrices  $\mathbf{G}_{sp}(\omega)$  and  $\mathbf{G}_{sc}(\omega)$  contain the frequency response functions (FRFs) between the sensors output signals and respectively the primary excitation and the control input signals, which can be expressed in terms of the following two matrix expressions:

$$\mathbf{G}_{sp}(\omega) = \boldsymbol{\sigma}_s(\omega) \mathbf{a}_p(\omega) \quad (17)$$

$$\mathbf{G}_{sc}(\omega) = \boldsymbol{\sigma}_s(\omega) \mathbf{A}_c(\omega) \quad (18)$$

For the structural sensors,  $\sigma_s(\omega)$  is a  $S \times N$  matrix with the modal sensing terms  $\sigma_s^{s,n}(\omega)$  generated by the sensor(s) fixed on the panel. More specifically, for the point MST accelerometers, they are simply given by the modal amplitudes at the positions of the sensors. Instead, for the distributed piezoelectric sensors shown in Table 2–5, they are given by more elaborate expressions, which correspond to those presented in Section 3 for the dual piezoelectric actuators. Alternatively, for the point microphone sensors located in front of the panel, they are given by the Rayleigh integral [6] of the sound radiated by a baffled planar surface weighted by the modal amplitudes. For instance, the sound measured by the  $s$ -th microphone for the vibration field of the  $n$ -th mode of the panel is given by

$$\sigma_s^{s,n}(\omega) = \frac{j\omega\rho_0}{2\pi} \int_0^{l_{xp}} \int_0^{l_{yp}} \varphi_n(x,y) \frac{e^{-jk_0R}}{R} dx dy \quad (19)$$

where  $R$  is the distance between the position of the  $s$ -th microphone  $(x_s, y_s, z_s)$  and the point of coordinates  $(x, y, 0)$  on the panel. In general, the terms in the matrix  $\sigma_s$  encompass the transfer function of the output signal conditioner. Thus, they may include a time-integrator and a high-pass filter to implement DC decoupling and a low-pass filter to attenuate the undesired effects produced by the electro-mechanical coupling between the sensors and actuators and by noise at higher frequencies than the selected 0–2 kHz range.

### 3.2 Feed-forward and feedback control architectures

As shown in the block diagrams reported in Table 2–5, the smart panels considered in this study are characterized by two control architectures: feed-forward and feedback. Feed-forward systems are normally used to control deterministic disturbances, for which a reference harmonic or periodic signal can be measured [6,21]. In contrast, feedback systems are usually employed to control stochastic disturbances such as diffuse sound fields or sound pressure fields generated by turbulent boundary layer aerodynamic excitations, which cannot be measured in advance to provide a reliable set of reference signals [6,32,38,99,100].

To start with, let's consider the smart panels depicted in Table 2, which implement multi-channels feed-forward controllers [6,21,22,25,38]. This control architecture relies on the advance knowledge of a reference signal  $r(\omega_0)$  correlated to the harmonic

disturbance to be canceled, which in this study is a time-harmonic plane wave with frequency  $\omega_0$ . According to the block diagram, the reference signal is fed to an array of control filters  $h_1(\omega_0), h_2(\omega_0), \dots, h_R(\omega_0)$ , which generate the control signals  $v_{c1}(\omega_0), v_{c2}(\omega_0), \dots, v_{cR}(\omega_0)$  driving the piezoelectric strain actuators embedded on the panel. Therefore, the vector with the  $R$  complex control signals can be expressed as

$$\mathbf{v}_c(\omega_0) = \mathbf{h}(\omega_0)r(\omega_0) \quad (20)$$

where  $\mathbf{h}(\omega_0)$  is the  $R \times 1$  vector with the control filters. These filters are normally set to minimize quadratic cost functions reconstructed from a set of error sensors. Therefore, in practice adaptive feed-forward control schemes are implemented [22,25], such that the control filters can be continuously adapted to minimize the objective quadratic cost function. Normally, the control filters are set to minimize the sum of the mean-square error signals measured by the array of sensors, such that  $J(\omega_0) = \sum_{s=1}^S |v_{ss}(\omega_0)|^2$ . In this case, considering Eqs. (20) and (16), the cost function can be expressed in terms of the following Hermitian quadratic matrix expression:

$$\begin{aligned} J(\omega_0) &= \sum_{s=1}^S |v_{ss}(\omega_0)|^2 = \mathbf{v}_s^H \mathbf{v}_s \\ &= \mathbf{h}^H \mathbf{G}_{sc}^H \mathbf{G}_{sc} \mathbf{h} + \mathbf{h}^H \mathbf{G}_{sc}^H \mathbf{G}_{sp} p_i + p_i^* \mathbf{G}_{sp}^H \mathbf{G}_{sc} \mathbf{h} + p_i^* \mathbf{G}_{sp}^H \mathbf{G}_{sp} p_i. \end{aligned} \quad (21)$$

As shown in Ref. [25] for example, the minimum of this quadratic cost function can be derived for three cases. First, the over-determined case with more sensors than actuators in which case:

$$\mathbf{h}_{opt} = -[\mathbf{G}_{sc}^H \mathbf{G}_{sc}]^{-1} \mathbf{G}_{sc}^H \mathbf{G}_{sp} p_i \quad (22a)$$

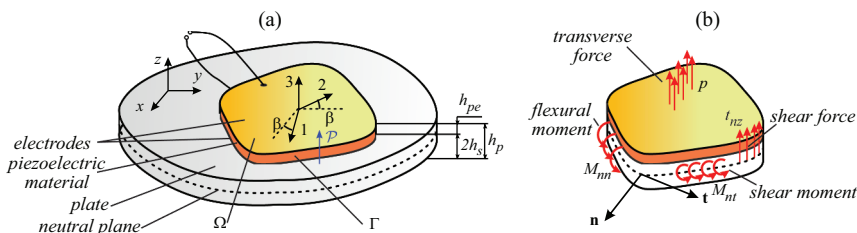
Second, the fully-determined case with equal numbers of sensors and actuators such that:

$$\mathbf{h}_{opt} = -\mathbf{G}_{sc}^{-1} \mathbf{G}_{sp} p_i \quad (22b)$$

Third, the under-determined case with fewer sensors than actuators [25], where:

$$\mathbf{h}_{opt} = -\mathbf{G}_{sc}^H [\mathbf{G}_{sc} \mathbf{G}_{sc}^H]^{-1} \mathbf{G}_{sp} p_i \quad (22c)$$

This formulation can be used also to study the single-channel control systems depicted in Table 3, although the matrix expressions will be replaced by simpler scalar formulae.



**Figure 5.** (a) Flat core structure and piezoelectric transducer. (b) Equivalent flexural excitations produced on the core structure by the piezoelectric transducer.

Let's now consider the smart panels depicted in Table 4, which implement multi-channel feedback controllers with an equal number of control actuators and error sensors such that  $R = S$ . As depicted in the block diagram, these arrangements implement a typical disturbance-rejection feedback architecture. Therefore, in this case, the vector with the  $R$  complex control signals is given by

$$\mathbf{v}_c(\omega) = -\mathbf{H}(\omega)\mathbf{v}_s(\omega) \quad (23)$$

where  $\mathbf{H}(\omega)$  is a fully populated matrix of control functions and  $\mathbf{v}_s$  is the vector with the  $S$  complex signals measured by the error sensors, which is given by Eq. (16). Therefore, substituting Eq. (23) in Eq. (16) the vector with the closed loop error signals is given by

$$\mathbf{v}_s(\omega) = [\mathbf{I} + \mathbf{G}_{sc}(\omega)\mathbf{H}(\omega)]^{-1}\mathbf{G}_{sp}(\omega)p_i(\omega) \quad (24)$$

where  $[\mathbf{I} + \mathbf{G}_{sc}(\omega)\mathbf{H}(\omega)]$  is the 'return difference matrix' [25]. The optimal design of the control functions is rather involved [38,39,46,47,101–111] and would require a reliable model of the plant responses between the  $S$  outputs from the error sensors and the  $R$  inputs to the control actuators, which compose the fully populated matrix  $\mathbf{G}_{sc}(\omega)$  [25,38,39,46,47]. Normally, the electro-mechanical response of smart structures is heavily affected by the operation conditions, such as for example temperature variations, tensioning effects, imposed constraints, etc. Therefore, the model for the plant responses should be continuously updated to take account the effective response of the smart structure [25,38,39,46,47]. Alternatively, robust control design should be implemented, which, however, would limit the effectiveness of the controller [25,38,39,46,47]. For this reason, simpler feedback control schemes are normally sought. In particular, this study considers the implementation of single channel or multi-channel decentralized velocity feedback loops between closely located and dual sensor-actuator pairs [25,46,47]. In this respect, Ref. [112], showed that, for the case of broadband flexural vibration control of thin structures with collocated and dual sensor-actuator pairs, multichannel decentralized feedback systems perform as well as distributed and centralized control systems. In decentralized feedback control systems, the control functions for each control loop can be designed using the classic feedback control theory, which is based on frequency domain analysis and synthesis [25,46,47,113–116]. In general, it can be demonstrated that, when the array of decentralized feedback loops is made with collocated and dual sensor-actuator pairs [117–119], the feedback loops are bound to be unconditionally stable [120,121], even for large variations of the response of the hosting structure or failure of single control units. Therefore, this control architecture has the advantage of being relatively simple and modular. The simplest type of collocated and dual sensor-actuator pair is given by a point velocity sensor and a collocated point force actuator. This sensor-actuator pair can be suitably used to implement a constant gain velocity feedback loop, which is physically equivalent to adding a sky-hook point damper to the hosting structure [6,40]. At low frequencies where the flexural response of the structure is dominated by the resonant responses of low order modes [6,23], adding sky-hook dampers can be very effective, both in terms of controlling the response and the sound transmission of the structure [6,40]. In principle, the control performance of the feedback loop can be further improved by tailoring the control function to the response of the hosting system. However, this would require again

a model of the system response and thus either on-line model updating or robust control design, which are not desirable. As will be discussed in details in Section 5, the practical sensor-actuator pairs considered in this study are not exactly collocated and dual. For this reason, the feedback controllers will normally include time-integrators, high-pass filters to avoid DC coupling between the transducers, low-pass filters to cut high-frequency undesired electro-dynamic effects of the smart structure and, in some cases, compensators designed to cut specific electro-dynamic effects of the transducers (e.g. shift to lower frequencies the resonant response of proof mass electromagnetic force actuators [53]). All these measures depend on the sensor-actuator transducers rather than the dynamic response of the hosting structure, and thus can be effectively designed upfront independently from the dynamic response of the hosting structure.

#### 4. Sensing and actuation effects produced by piezoelectric transducers

As shown in the sketches of Table 2–5, part of the smart panels considered in this study are composed by a core substrate, that is a thin aluminum panel, with piezoelectric strain sensors and piezoelectric strain actuators bonded on the top and bottom surfaces respectively. More specifically, two types of transducers are considered, that is: first, dense arrays of small patches made with piezoceramic PZT materials (led, zirconate, titanate [122]) and, second, large foils that cover the whole surface of the panel made with PVDF materials (polyvinylidene fluoride polymer [123]).

As shown in Figure 5, both types of transducers are formed by a thin layer of piezoelectric material poled in transverse direction with thin electrodes deposited on either side. The passive mechanical effects produced either by the arrays of small patches or by the large piezoelectric films are taken into account as smeared mass and smeared bending stiffness effects. Therefore, the equation of motion for the flexural vibration of the composite structure has been derived with reference to the classical laminated plate theory, which is an extension of Kirchhoff plate theory for thin plates [5,124,125]. Accordingly, a plane stress state is assumed such that the constitutive equations for the core substrate and for the outer piezoelectric layers are given by the following expressions [5,126–128]:

$$\begin{bmatrix} T_1 \\ T_2 \\ T_6 \end{bmatrix} = \begin{bmatrix} \frac{E_s}{1-\nu_s^2} & \frac{\nu_s E_s}{1-\nu_s^2} & 0 \\ \frac{\nu_s E_s}{1-\nu_s^2} & \frac{E_s}{1-\nu_s^2} & 0 \\ 0 & 0 & \frac{E_s}{2(1+\nu_s)} \end{bmatrix} \begin{bmatrix} S_1 \\ S_2 \\ S_6 \end{bmatrix} \quad (25)$$

for the metal core layer and

$$\begin{bmatrix} T_1 \\ T_2 \\ T_6 \end{bmatrix} = \begin{bmatrix} \frac{E_{pe}}{1-\nu_{pe}^2} & \frac{\nu_{pe} E_{pe}}{1-\nu_{pe}^2} & 0 \\ \frac{\nu_{pe} E_{pe}}{1-\nu_{pe}^2} & \frac{E_{pe}}{1-\nu_{pe}^2} & 0 \\ 0 & 0 & \frac{E_{pe}}{2(1+\nu_{pe})} \end{bmatrix} \begin{bmatrix} S_1 \\ S_2 \\ S_6 \end{bmatrix} - \begin{bmatrix} e_{31}^0 \\ e_{32}^0 \\ e_{36}^0 \end{bmatrix} E_3 \quad (26)$$

$$D_3 = \epsilon_{33}E_3 + \begin{bmatrix} d_{31}^0 & d_{32}^0 & d_{36}^0 \end{bmatrix} \begin{bmatrix} T_1 \\ T_2 \\ T_6 \end{bmatrix} \quad (27)$$

for the outer piezoelectric layers. In these expressions,  $S_1, S_2, S_6$  and  $T_1, T_2, T_6$  are the strain and stress components for flexural vibrations of the thin layers, which assume plain strain deformation, such that  $S_3 = S_4 = S_5 = 0$  and  $T_3 = T_4 = T_5 = 0$ , where  $S_1, \dots, S_6$  and  $T_1, \dots, T_6$  are the extension and shear strain components and the normal and shear stress components respectively, defined with respect to the Voigt-Kelvin notation [124]. Also,  $\rho_s, E_s, \nu_s$ , and  $\rho_{pe}, E_{pe}, \nu_{pe}$  are the densities, Young's modulus of elasticity and Poisson ratio of the core substrate, i.e. aluminum plate, and outer piezoelectric layers respectively. Also,  $E_3$  is the electric field generated by the electric potential difference  $V_3$  between the electrodes and  $D_3$  is the electric displacement collected by the two electrodes. Moreover,  $\epsilon_{33}$  is the permittivity of the piezoelectric material in direction 3. Finally  $e_{31}^0, e_{32}^0$ , and  $e_{36}^0$  are the piezoelectric stress/charge constants, which for a thin piezoelectric layer can be expressed in terms of the following law [128]:

$$\begin{bmatrix} e_{31}^0 \\ e_{32}^0 \\ e_{36}^0 \end{bmatrix} = \begin{bmatrix} m^2 & n^2 & -2mn \\ n^2 & m^2 & 2mn \\ mn & -mn & m^2 - n^2 \end{bmatrix} \begin{bmatrix} \frac{E_{pe}}{1-\nu_{pe}^2} & \frac{\nu_{pe}E_{pe}}{1-\nu_{pe}^2} & 0 \\ \frac{\nu_{pe}E_{pe}}{1-\nu_{pe}^2} & \frac{E_{pe}}{1-\nu_{pe}^2} & 0 \\ 0 & 0 & \frac{E_{pe}}{2(1+\nu_{pe})} \end{bmatrix} \begin{bmatrix} d_{31}^0 \\ d_{32}^0 \\ d_{36}^0 \end{bmatrix} \quad (28)$$

Here  $m = \cos \beta$ ,  $n = \sin \beta$ , where, according to Figure 5(a),  $\beta$  is the angle between the principal axis 1,2 of the piezoelectric material and the principal axis  $x,y$  of the panel respectively. Also,  $d_{31}^0, d_{32}^0$ , and  $d_{36}^0$  are the piezoelectric strain/charge constants [128], whose typical values for PZT and PVDF materials are summarized in Table 1.

Since the study is focused on sound transmission in the 0–2 kHz frequency band, only the flexural response of the smart panels is considered in this study. Therefore, the sensing and actuation effects of the piezoelectric strain transducers are modeled using the formulations proposed by Lee [128] and Deraemaeker *et al.* [129] with respect to flexural vibrations only. In this respect, it is important to highlight that, although in-plane vibrations have negligible effects on the sound transmission, they actually highly influence the coupled response between strain sensors and strain actuators pairs. This is particularly the case for matched sensor-actuator pairs formed by large piezoelectric patches or foils bonded on the two faces of the core thin structure. In this case, the study presented in Ref. [27] showed that, above a given cutoff frequency, the coupling between sensors and actuators via in-plane extensional and shear vibrations may exceed that via out-of-plane flexural vibrations. This is quite a critical problem, both because the control system would drive the actuators to control the in-plane vibrations rather than the flexural vibrations and because the control system may actually become unstable. Indeed, the study in Ref. [27], showed that the sensor-actuator couplings via in-plane and out-of-plane vibrations are actually out-of-phase and thus the sensor-actuator Frequency Response Function (FRF) cannot be minimum phase. Hence, according to the Nyquist stability criterion [25], the control system cannot be unconditionally stable.

Some panels use arrays of lightweight miniaturized MST seismic accelerometers, which produce negligible effects on the dynamic response of the panel in the 0–2 kHz frequency band considered in this study. Therefore, the accelerometers are modeled as idealized

point sensors. Again, it is important highlight that, the stability of the proposed control systems relies on the sensor-actuator FRF over a wide frequency range, which would encompass the typical resonance peak and  $180^{\circ}$  phase lag effects produced by the second order response of the seismic accelerometers [35,44]. Thus, in this case too, the sensor-actuator FRF cannot be minimum-phase such that, according to Nyquist stability criterion, the control system cannot be guaranteed unconditionally stable. Similar considerations should be made for the panels with arrays of small-scale proof-mass electromagnetic actuators, which are characterized by a resonant response that greatly affects the stability of the feedback loops too [30,34,37,45].

#### 4.1 Piezoelectric sensor bonded on a thin core structure

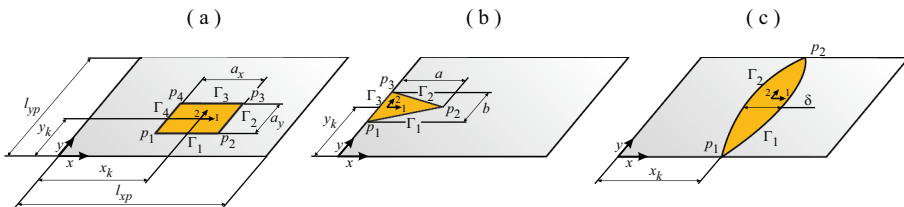
In general, when a piezoelectric patch or foil poled in transverse direction is bonded onto the surface of a thin structure, the out-of-plane flexural vibration and the in-plane extensional and shear vibrations of the structure stretch and twist the piezoelectric material, which then displaces charges on the surfaces of the two electrodes by means of the direct piezoelectric effect [130]. A current output signal proportional to the transducer strain rate can thus be obtained with an appropriate charge amplifier signal conditioner. As shown in the sketch (a) of Figure 5, the electrical output of the piezoelectric sensor is taken along axis 3 with reference to strain of the piezoelectric material along axis 1 and 2. The current output signal  $i_s(t)$  generated by a piezoelectric transducer bonded to a thin flat plate can be expressed in terms of two components. The first is due to the out-of-plane flexural vibration of the structure,  $i_{s,b}(t)$  whereas the second is due to the in-plane extensional and shear vibrations of the structure,  $i_{s,a}(t)$ . Therefore:

$$i_s(t) = i_{s,b}(t) + i_{s,a}(t) \quad (29)$$

where, according to Refs. [6,128],

$$i_{s,b}(t) = -\frac{h_p}{2} \begin{matrix} l_{xp} & l_{yp} \\ 0 & 0 \end{matrix} S(x,y) \left[ e_{31}^0 \frac{\partial^2 \dot{w}(x,y,t)}{\partial x^2} + e_{32}^0 \frac{\partial^2 \dot{w}(x,y,t)}{\partial y^2} + 2e_{36}^0 \frac{\partial^2 \dot{w}(x,y,t)}{\partial x \partial y} \right] dx dy \quad (30)$$

$$i_{s,a}(t) = \begin{matrix} l_{xp} & l_{yp} \\ 0 & 0 \end{matrix} S(x,y) \left[ e_{31}^0 \frac{\partial \dot{u}(x,y,t)}{\partial x} + e_{32}^0 \frac{\partial \dot{v}(x,y,t)}{\partial y} + e_{36}^0 \left( \frac{\partial \dot{u}(x,y,t)}{\partial y} + \frac{\partial \dot{v}(x,y,t)}{\partial x} \right) \right] dx dy \quad (31)$$



**Figure 6.** Rectangular panels with (a) square, (b) triangular, and (c) quadratic strip piezoelectric patches.

Here  $h_p = h_s + h_{pe}$  is given by the thickness of the core substrate  $h_s$  and the thickness of the piezoelectric layer  $h_{pe}$ . Also,  $\dot{u}(x, y, t)$ ,  $\dot{v}(x, y, t)$  and  $\dot{w}(x, y, t)$  are the velocities of the plate along the  $x$ ,  $y$  and  $z$  directions. Finally,  $S(x, y) = F(x, y)P_0(x, y)$  is a sensitivity function, which, according to Lee's formulation [128], is given by the product of the spatial function  $F(x, y)$ , which provides the surface of the electrodes deposited on the piezoelectric material, and the poling function  $P_0(x, y)$ , which provides the strength of the polarization in directions 1,2,6, over the surface of the piezoelectric material, i.e.  $P_0(x, y) = P_1(x, y) = P_2(x, y) = P_6(x, y)$ . According to Eq. (28), an orthotropic piezoelectric material with strain/charge constants  $d_{31}^0 \neq d_{32}^0$  and  $d_{36}^0 = 0$  would be characterized by three stress/charge constants, i.e.  $e_{31}^0 \neq 0$ ,  $e_{32}^0 \neq 0$ ,  $e_{36}^0 \neq 0$ , provided its principal axes 1,2 are oriented at an angle  $\beta \neq 0$  with respect to the principal axes  $x, y$  of the core panel. Therefore, the sensor output current will result both from the transducer extensional strains in directions 1,2 and from the shear strain in direction 6, which can be generated respectively by bending and twisting deformations of the composite structure. Instead, a plane isotropic piezoelectric material with strain/charge constants  $d_{31}^0 = d_{32}^0$  and  $d_{36}^0 = 0$  will always be characterized only by two stress/charge constants, i.e.  $e_{31}^0 \neq 0$ ,  $e_{32}^0 \neq 0$ ,  $e_{36}^0 = 0$ ; regardless the principal axes 1,2 are oriented at an angle  $\beta \neq 0$  with respect to the principal axes  $x, y$  of the core panel. In other words, the current output of the transducer will solely depend on the bending deformation of the composite structure.

#### 4.2 Piezoelectric actuator bonded on a thin core structure

In general, when an electric potential difference  $V_3$  is applied between the electrodes of a piezoelectric patch or foil poled in transverse direction, the electric field generated across the piezoelectric material infer a plane strain effect by means of the inverse piezoelectric effect [130]. When the piezoelectric patch or foil is bonded on the thin core structure, a force field is generated, which bends, twists and stretches the composite structure [128]. The equations of motion for the in-plane extensional and shear vibrations and for the uncoupled out-of-plane flexural vibration are in this case given by [6,128]:

$$\frac{E_p h_p}{1 - \nu_p^2} \left( \frac{\partial^2 u}{\partial x^2} + \frac{1 - \nu_p}{2} \frac{\partial^2 u}{\partial y^2} \right) + \frac{E_p h_p}{2(1 - \nu_p)} \frac{\partial^2 v}{\partial x \partial y} - \rho_p h_p \frac{\partial^2 u}{\partial t^2} = \delta_{ep} \left( e_{31}^0 \frac{\partial S}{\partial x} + e_{36}^0 \frac{\partial S}{\partial y} \right) v_c \quad (32)$$

$$\frac{E_p h_p}{2(1 - \nu_p)} \frac{\partial^2 u}{\partial x \partial y} + \frac{E_p h_p}{1 - \nu_p^2} \left( \frac{1 - \nu_p}{2} \frac{\partial^2 v}{\partial x^2} + \frac{\partial^2 v}{\partial y^2} \right) - \rho_p h_p \frac{\partial^2 v}{\partial t^2} = \delta_{ep} \left( e_{36}^0 \frac{\partial S}{\partial x} + e_{32}^0 \frac{\partial S}{\partial y} \right) v_c \quad (33)$$

$$\begin{aligned} & \frac{E_p h_p^3}{12(1 - \nu_p^2)} \left( \frac{\partial^4 w}{\partial x^4} + 2 \frac{\partial^4 w}{\partial x^2 \partial y^2} + \frac{\partial^4 w}{\partial y^4} \right) + \rho_p h_p \frac{\partial^2 w}{\partial t^2} \\ & = - \frac{h_p}{2} \delta_{ep} \left( e_{31}^0 \frac{\partial^2 S}{\partial x^2} + 2e_{36}^0 \frac{\partial^2 S}{\partial x \partial y} + e_{32}^0 \frac{\partial^2 S}{\partial y^2} \right) v_c \end{aligned} \quad (34)$$

where  $\rho_p$ ,  $E_p$ ,  $\nu_p$  are the averaged density, Young's modulus of elasticity and Poisson ratio of the composite structure,  $v_c$  is the control voltage applied across the piezoelectric transducer and  $\delta_{ep}$  is equal to  $\pm 1$  when the electric field and poling direction point in the same or opposite directions respectively. As seen for the sensor Eqs. (30), (31),  $h_p =$

$h_s + h_{pe}$  is given by the thickness of the metal core substrate  $h_s$  and the thickness of the piezoelectric layer  $h_{pe}$ .

### 4.3 Shading of piezoelectric sensor and actuator transducers

The expressions derived in Eqs. (30), (31) and (32), (33), (34) in the previous two sections showed that the sensing and actuation effects produced by thin piezoelectric patches or foils bonded on a metallic core layer depend on the so called sensitivity function  $S(x, y) = F(x, y)P_0(x, y)$ , which is composed by two functions [128]. The first defines the surface covered by the electrodes of the piezoelectric transducers  $F(x, y)$ , that is the effective area where the piezoelectric sensing and actuation effects take place. The second defines the strength of the poling in transverse direction, i.e.  $P_3(x, y)$ , which for simplicity has been taken constant and equal to  $P_0(x, y) = P_3(x, y)$ . Therefore the sensing and actuation effects described in the previous two sections depend on the shape of the electrodes deposited on the two faces of the thin piezoelectric transducers. In other words, the shape of the electrodes determines the regions where the charges produced by the direct piezoelectric effect are collected and the regions where a stress field is generated by the inverse piezoelectric effect. The sensing and actuation effects are normally expressed with respect to equivalent distributed velocity and excitation functions [27,28,87,88,128,129,131–135]. Initially, these equivalent functions were formulated using the so-called ‘theory of distributions’, which, however, led to incongruous results [35,129]. Also analytical solutions were derived from a Fourier transformation method combined with discretised higher order partial differential unit step function equations

Table 6. Contour and jump functions for the patches shown in Figure 6.

Actuator type	Contour	$n_x$	$n_y$	$n_x n_y$	$n_x^2$	$n_y^2$	Vertex	$[n_x n_y]$	$[n_x^2]$
Square patch Figure 6(a)	$\Gamma_1$	0	-1	0	0	1	$p_1$	0	1
	$\Gamma_2$	1	0	0	1	0	$p_2$	0	-1
	$\Gamma_3$	0	1	0	0	1	$p_3$	0	1
	$\Gamma_4$	-1	0	0	1	0	$p_4$	0	-1
Triangular patch Figure 6(b)	$\Gamma_1$	$\frac{b}{\Delta_t}$	$-\frac{2a}{\Delta_t}$	$-\frac{2ab}{\Delta_t^2}$	$\frac{b^2}{\Delta_t^2}$	$\frac{4a^2}{\Delta_t^2}$	$p_1$	$\frac{2ab}{\Delta_t^2}$	$1 - \frac{b^2}{\Delta_t^2}$
	$\Gamma_2$	$\frac{b}{\Delta_t}$	$\frac{2a}{\Delta_t}$	$\frac{2ab}{\Delta_t^2}$	$\frac{b^2}{\Delta_t^2}$	$\frac{4a^2}{\Delta_t^2}$	$p_2$	$-\frac{4ab}{\Delta_t^2}$	0
	$\Gamma_3$	-1	0	0	1	0	$p_3$	$\frac{2ab}{\Delta_t^2}$	$\frac{b^2}{\Delta_t^2} - 1$
Quadratic strip Figure 6(c)	$\Gamma_1$	$-\frac{1}{\Delta_s}$	$-\frac{m}{\Delta_s}$	$-\frac{m}{\Delta_s^2}$	$\frac{1}{\Delta_s^2}$	$\frac{m^2}{\Delta_s^2}$	$p_1$	$\frac{2rl_{yp}}{1+r^2l_{yp}^2}$	0
	$\Gamma_2$	$\frac{1}{\Delta_s}$	$-\frac{m}{\Delta_s}$	$-\frac{m}{\Delta_s^2}$	$\frac{1}{\Delta_s^2}$	$\frac{m^2}{\Delta_s^2}$	$p_2$	$\frac{2rl_{yp}}{1+r^2l_{yp}^2}$	0

$$\Delta_t = \sqrt{b^2 + 4a^2}, m = r(l_{yp}y - y^2), r = 2\delta/l_{yp}, \Delta_s = \sqrt{1 + r^2(l_{yp} - 2y)^2}$$

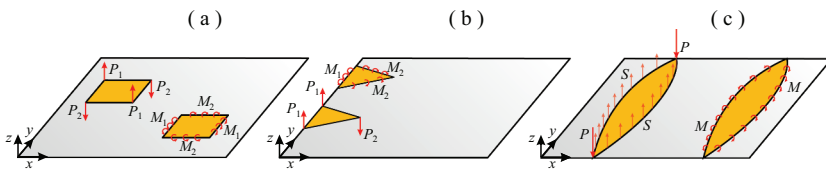


Figure 7. Sensing and excitation effects of the (a) square, (b) triangular, and (c) quadratic piezoelectric transducers bonded on a rectangular thin panel.



[136]. In parallel, finite element formulations were also developed [137,138]. In this paper, the bending equivalent loads produced by a piezoelectric transducer having electrodes with equivalent surface function  $F(x, y)$  are derived following the formulation proposed by Deraemaeker *et al.* [129]. The flexural sensing effects can also be derived with the same formulation. Actually, for equivalent sensitivity functions  $S(x, y)$ , they are given by the same expressions as those for the equivalent loads; therefore they are not specifically discussed in this paper. According to Figure 6, three geometries of the transducers are discussed: (a) rectangular, (b) triangular, and (c) array of quadratically shaped leafs. The piezoelectric materials are assumed orthotropic with strain/charge constants  $d_{31}^0 \neq d_{32}^0$  and  $d_{36}^0 = 0$ .

Since the study is focused on the flexural vibration and the sound transmission of the smart panels, the formulation for the flexural equivalent excitations produced by the piezoelectric transducers bonded on a thin flat plate core structure is considered only. The formulation proposed in Ref. [129] is based on Hamilton's principle and either Green's theorem or theory of distribution in two dimensions, where the perimeter of the electrode surface  $\Omega$  is defined by a contour function  $\Gamma$  characterized by discontinuity points. The equivalent loads are given by the following three contributes:

$$-p(x, y) = \frac{\partial^2}{\partial x^2} (h_p e_{31}^0 v_c) + \frac{\partial^2}{\partial y^2} (h_p e_{32}^0 v_c) + 2 \frac{\partial^2}{\partial x \partial y} (h_p e_{36}^0 v_c) \quad (35)$$

$$\begin{aligned} - \left( -\frac{\partial M_{nt}}{\partial s} + t_{nz} \right) &= ((e_{32}^0 - e_{31}^0) [n_x n_y]_i + 2e_{36}^0 [n_x^2]_i) h_p v_c \\ &+ \frac{\partial}{\partial s} \{ ((e_{32}^0 - e_{31}^0) n_x n_y + 2e_{36}^0 n_x^2) h_p v_c \} + \frac{\partial}{\partial x} (h_p e_{31}^0 v_c) n_x \\ &+ \frac{\partial}{\partial y} (h_p e_{32}^0 v_c) n_y + 2 \frac{\partial}{\partial x} (h_p e_{36}^0 v_c) n_y \end{aligned} \quad (36)$$

$$-M_{nn} = (e_{31}^0 n_x^2 + e_{32}^0 n_y^2 + 2e_{36}^0 n_x n_y) h_p v_c \quad (37)$$

Here  $[n_x^2]$  and  $[n_x n_y]$  are the discontinuity jumps of  $n_x^2$  and  $n_x n_y$ , where  $n_x$  and  $n_y$  are the  $x$  and  $y$  components of the unit vector  $\mathbf{n}$  normal to the contour  $\Gamma$ , which gives the effective surface electrode function  $F(x, y)$ . The discontinuity jump at position  $p(s) \in \Gamma$  of a given function  $g$  is defined as follows:  $[g]_p = g(p^+) - g(p^-)$  with  $p^+(s) = p(s + \delta)$  and  $p^-(s) = p(s - \delta)$  for  $\delta \rightarrow 0$ . Lastly  $\partial(\cdot)/\partial s$  is the derivative with respect to the curvilinear coordinate along the contour  $\Gamma$ . As shown in sketch (b) of Figure 5, the first term  $p(x, y)$  represents a surface pressure excitation generated when the thickness, the piezoelectric stress/charge parameters and the applied voltage have a non-uniform surface distribution over the electrodes. The second term  $(-\frac{\partial M_{nt}}{\partial s} + t_{nz})$ , provides the 'generalized or effective shear forces' along the contour  $\Gamma$ . In particular, the term  $((e_{32}^0 - e_{31}^0) [n_x n_y]_i + 2e_{36}^0 [n_x^2]_i) h_p v_c$  gives the effective shear force at discontinuity points  $p_i$  of the contour  $\Gamma$ . Finally, the third term  $M_{nn}$  gives the flexural moments, distributed along the contour  $\Gamma$ , which are oriented parallel to the tangent of  $\Gamma$ .

#### 4.3.1 Rectangular piezoelectric patch with arbitrary orientation of the principal axes

First, the flexural excitation field produced by a rectangular piezoelectric patch bonded on the thin core panel is considered. According to Figure 6(a) the lateral edges of the patch are aligned with the lateral edges of the panel. However, the principal axis 1,2 of the piezoelectric material are oriented with at an angle  $\beta$  to the axis  $x,y$  of the plate respectively. In this case, the contour function  $\Gamma$  for the perimeter of the rectangular patch can be expressed by four straight-line functions defined over specific domains:

$$\Gamma_{1,3} : \quad y(x) = y_k \mp \frac{a_y}{2} \quad \text{over} \quad x \in \left[ x_k - \frac{a_x}{2}, x_k + \frac{a_x}{2} \right] \quad (38a, b)$$

$$\Gamma_{2,4} : \quad x(y) = x_k \mp \frac{a_x}{2} \quad \text{over} \quad y \in \left[ y_k - \frac{a_y}{2}, y_k + \frac{a_y}{2} \right] \quad (38c, d)$$

The four line functions are joined at the following discontinuity points

$$p_{1,2,3,4}(x, y) = \left( x_k \mp \frac{a_x}{2}, y_k \mp \frac{a_y}{2} \right) \quad (39)$$

In summary, this contour function is characterized by the four normal functions along the edges of the patch and by four discontinuity jumps at the four corners of the piezoelectric patch, which are summarized in Table 6. Therefore, according to Eqs. (35)–(37), as shown in the sketch (a) of Figure 7, the flexural excitation field produced by a square piezoelectric patch is characterized by four shear forces at the corners [129]:

$$\left( -\frac{\partial M_{nt}}{\partial s} + t_{nz} \right) = \begin{cases} P_1 = +2e_{36}^0 h_p v_C & \text{at points } p_2 \text{ and } p_4 \\ P_2 = -2e_{36}^0 h_p v_C & \text{at points } p_1 \text{ and } p_3 \end{cases} \quad (40a, b)$$

and by four lines of bending moments along the edges [129]:

$$M_{nn} = \begin{cases} M_1 = -e_{31}^0 h_p v_C & \text{on the edges } \Gamma_2 \text{ and } \Gamma_4 \\ M_2 = -e_{32}^0 h_p v_C & \text{on the edges } \Gamma_1 \text{ and } \Gamma_3 \end{cases} \quad (41a, b)$$

According to Eqs. (40a,b), the shear forces at the four corners of the patch depend on the twisting stress/charge parameter  $e_{36}^0$ . Therefore, recalling Eq. (28), these forces are non-zero if the piezoelectric patch is made of an orthotropic material having the principal axis 1,2 oriented at an angle  $\beta \neq 0$  with respect to the plate principal axis  $x,y$  respectively and, also,  $d_{36}^0 \neq 0$  and/or  $d_{31}^0 \neq d_{32}^0$ . A rectangular patch made with a plane isotropic piezoelectric material such that  $d_{31}^0 = d_{32}^0$  and  $d_{36}^0 = 0$  is characterized by a null 36 stress/charge constant, i.e.  $e_{36}^0 = 0$ . Therefore it cannot generate a twisting stress/charge effect, that is the point shear forces at the corners of the patch, regardless the piezoelectric material principal axis 1,2 are or are not aligned with the structure principal axis  $x,y$  respectively. Eqs. (40a,b) indicate that the shear forces at the corners of the patch have equal modulus and opposite sign in pairs, that is  $P_1 = -P_2$ . Therefore, the shear forces at the four corners of the patch balance out so that, as one would expect for a strain actuator, no net transverse force is produced on the panel.

### 4.3.2 Triangular piezoelectric patch with principal axes parallel to the core panel structure principal axes

Next, the flexural excitation field produced by a triangular piezoelectric patch bonded on the thin panel is considered. As shown in [Figure 6\(b\)](#), the case is considered where the patch has isosceles triangular shape with the base edge aligned with the edge  $x = 0$  of the panel. The piezoelectric material has principal axes 1,2 parallel to the  $x,y$  principal axes of the core plate structure. Therefore, the contour function  $\Gamma$  that delimits the surface of the triangular piezoelectric transducer can be represented in terms of the following three straight-line functions defined over specific domains

$$\Gamma_{1,2} : \quad y(x) = y_k \mp \frac{b}{2} \pm mx \quad \text{over} \quad x \in [0, a] \quad (42a, b)$$

$$\Gamma_3 : \quad x(y) = 0 \quad \text{over} \quad y \in \left[ y_k - \frac{b}{2}, y_k + \frac{b}{2} \right] \quad (42c)$$

Here  $m = \frac{b}{2a}$  is the slope coefficient of the lateral edges. The three line functions are joined at the following discontinuity points

$$p_1(x, y) = \left( 0, y_k - \frac{b}{2} \right) \quad (43a)$$

$$p_2(x, y) = (a, y_k) \quad (43b)$$

$$p_3(x, y) = \left( 0, y_k + \frac{b}{2} \right) \quad (43c)$$

This contour function is characterized by the three normal functions along the edges of the triangular patch and by three discontinuity jumps at the three corners of the patch, which are summarized in [Table 6](#). Hence, based on Eqs. (33)–(35) and sketch (b) of [Figure 7](#), the flexural excitation field produce by a triangular piezoelectric patch is characterized by three shear forces at the corners [[129](#)]:

$$\left( -\frac{\partial M_{nt}}{\partial S} + t_{nz} \right) = \begin{cases} P_1 = + (e_{32}^0 - e_{31}^0) \frac{2ba}{b^2+4a^2} h_p v_C & \text{at points } p_1 \\ P_2 = - (e_{32}^0 - e_{31}^0) \frac{4ba}{b^2+4a^2} h_p v_C & \text{at points } p_2 \\ P_3 = + (e_{32}^0 - e_{31}^0) \frac{2ba}{b^2+4a^2} h_p v_C & \text{at points } p_3 \end{cases} \quad (44a, b, c)$$

and by three lines of bending moments along the edges [[129](#)]:

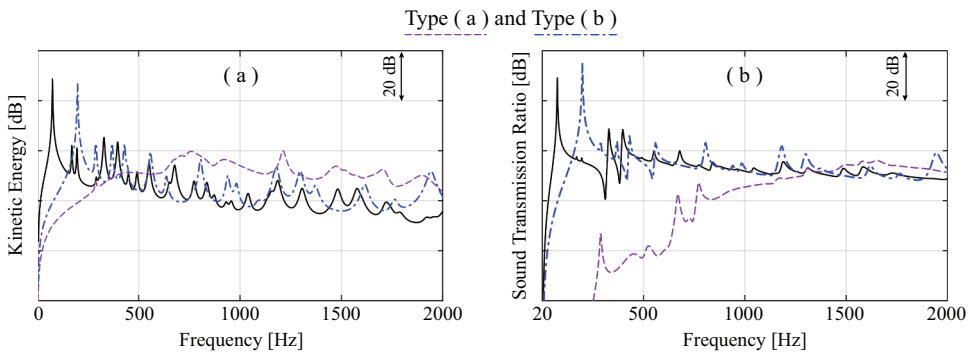
$$M_{nn} = \begin{cases} M_1 = -\frac{b^2 e_{31}^0 + 4a^2 e_{32}^0}{b^2 + 4a^2} h_p v_C & \text{on the edge } \Gamma_1 \\ M_1 = -\frac{b^2 e_{31}^0 + 4a^2 e_{32}^0}{b^2 + 4a^2} h_p v_C & \text{on the edge } \Gamma_2 \\ M_2 = -e_{31}^0 h_p v_C & \text{on the edge } \Gamma_3 \end{cases} \quad (45a, b, c)$$

In this case, according to Eqs. (44a-c), the shear forces at the three corners of the patch depend on the difference between the extensional stress/charge parameters  $e_{31}^0$  and  $e_{32}^0$ . Therefore, when the triangular patch is made of an orthotropic piezoelectric material with  $d_{31}^0 \neq d_{32}^0$ , regardless the principal axes 1,2 of the patch are or are not parallel to  $x,y$  principal axes of the core panel structure, point shear forces are generated at the three

vertices. This arises from the fact that the two lateral edges of the patch are oblique with respect to the principal axis of the piezoelectric material. As shown in the sketch (b) of Figure 7, the shear forces at the vertices of the triangular patch are linked by the following relation:  $P_2 = -2P_1$ . Therefore, also in this case, the total transverse point force generated on the panel by the three shear forces at the vertices of the triangular patch is null, as one would expect from a strain transducer. Nevertheless, as sketched in Figure 7(b), when the patch is bonded with the base edge over the lateral edge of a constrained panel, the shear point forces generated at the base vertices of the triangle are balanced by the reaction forces exerted along the border of the panel. In this way, a net point shear force  $P_2$  is generated at the tip of the triangular patch. This is a very interesting effect, which could be used to make an effective velocity feedback control loop with a ‘quasi’ collocated and dual sensor-actuator arrangement. For instance, an accelerometer sensor could be placed at the tip of the triangular actuator to form a collocated and dual point force and velocity sensor pair [29,35]. In this case, the open loop sensor-actuator FRF is bound to be minimum phase [25] such that the feedback loop would be unconditionally stable. In practice, the bending moments generated along the lateral edges of the triangular patch tend to disrupt these properties. Nevertheless, a careful design of the triangular patch could lead a configuration where the flexural excitation due to the shear point force generated at the tip of the triangular patch is much larger than the flexural excitation exerted by the bending moments generated along the lateral edges such that the feedback loop could implement large control gains [35].

#### 4.3.3 Piezoelectric foil with principal axes parallel to the core panel structure principal axes and quadratically shaded electrodes

Finally, the flexural excitation field produced by a piezoelectric foil with quadratically shaded electrodes is considered. According to sketches (i), (j), and (q) in Tables 4 and 5, the piezoelectric foil is covered by electrodes formed by an array of strips with quadratic edges. In this section, as shown in Figure 6(c), the flexural excitation field produced by the  $k$ -th strip centered at  $x_k$  is considered. The  $k$ -th strip can be described by the following two quadratic functions [28]:



**Figure 8.** Flexural kinetic energy (a) and sound transmission ratio (b) for the smart panels with the feed-forward control systems Type (a) (purple dashed lines) and Type (b) (blue dash-dotted lines) shown in Table 2.

$$\Gamma_{1,2}: \quad x(y) = x_k \mp r(l_{yp}y - y^2) \quad \text{over} \quad y \in [0, l_{yp}] \quad (46a, b)$$

Here  $r = \frac{2\delta}{l_{yp}}$ , where  $\delta$  is the width of the strips and  $x_k$  is the coordinate of the  $y$ -axis of symmetry of the  $k$ -th strip. The two quadratic functions  $\Gamma_1$  and  $\Gamma_2$ , which define the quadratic edges of the strip, are connected at two discontinuity points:

$$p_1(x, y) = (x_k, 0), \quad (47a)$$

$$p_2(x, y) = (x_k, l_{yp}) \quad (47b)$$

The contour function is thus characterized by the two normal functions along the edges of the electrodes and by the two discontinuity jumps at the vertices of the strip reported in Table 6. Accordingly, considering Eqs. (35)–(37) and sketch (c) of Figure 7, the flexural excitation field produce by a quadratic leaf is characterized by the following shear forces at the vertices of the strip

$$\left( -\frac{\partial M_{nt}}{\partial s} + t_{nz} \right) = \begin{cases} P = -(e_{32}^0 - e_{31}^0) \frac{2rl_{yp}}{1+r^2l_{yp}^2} h_p v_C & \text{at point } p_1 \\ P = -(e_{32}^0 - e_{31}^0) \frac{2rl_{yp}}{1+r^2l_{yp}^2} h_p v_C & \text{at points } p_2 \end{cases} \quad (48a, b)$$

Also, the following lines of shear forces are generated along the two quadratic edges:

$$\left( -\frac{\partial M_{nt}}{\partial s} + t_{nz} \right) = \begin{cases} S = +(e_{31}^0 - e_{32}^0) \frac{2r(1-r^2(l_{yp}-2y)^2)}{(1+r^2(l_{yp}-2y)^2)^{5/2}} h_p v_C & \text{on the edge } \Gamma_1 \\ S = +(e_{31}^0 - e_{32}^0) \frac{2r(1-r^2(l_{yp}-2y)^2)}{(1+r^2(l_{yp}-2y)^2)^{5/2}} h_p v_C & \text{on the edge } \Gamma_2 \end{cases} \quad (49a, b)$$

Moreover, the following lines of bending moments are produced along the two quadratic edges:

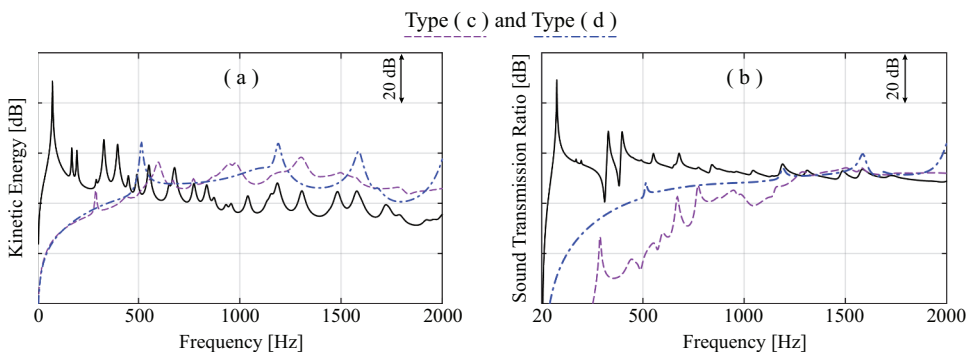
$$M_{nn} = \begin{cases} M = -\frac{e_{31}^0 r^2 (l_{yp}-2y)^2 + e_{32}^0}{1+r^2(l_{yp}-2y)^2} h_p v_C & \text{on the edge } \Gamma_1 \\ M = -\frac{e_{31}^0 r^2 (l_{yp}-2y)^2 + e_{32}^0}{1+r^2(l_{yp}-2y)^2} h_p v_C & \text{on the edge } \Gamma_2 \end{cases} \quad (50a, b)$$

Based on Eqs. (47a,b) and (49a,b), in this case too, the shear forces depend on the difference between the extensional stress/charge parameters  $e_{31}^0$  and  $e_{32}^0$ . Therefore, irrespectively the principal axes 1,2 of the piezoelectric material are parallel to  $x,y$  principal axes of the panel, when the piezoelectric foil is made of an orthotropic piezoelectric material with  $d_{31}^0 \neq d_{32}^0$ , point and line shear forces are generated at the two vertices and along the two edges of the strip respectively. Moreover, as expected for a strain actuator, there is no net transverse force since the point shear forces at the vertices are balanced by the line forces along the two quadratic edges, that is  $\int_{\Gamma_1} S ds + \int_{\Gamma_2} S ds = -2P$ . In summary, as shown in Figure 7(c), for a constrained panel, a strip produces along the quadratic lateral edges lines of shear forces and lines of bending moments. When, as shown in sketches (i), (j), and (q) in Tables 4 and 5, the piezoelectric foil is covered by a dense array of quadratically shaded electrodes, a dense array of line bending excitations is produced, whose effect approximate a uniform transverse bending excitation. More specifically, a uniform force-like excitation is produced over the panel, which can be used to excite

the volumetric flexural vibration of the panel. Therefore, this type of transducer can be effectively exploited in feedforward and feedback systems set to control the sound transmission [28,58]. Actually, a matched piezoelectric sensor with quadratically shaded electrodes could be bonded on the other face of the panel to get a sensor-actuator pair specifically tailored to control the volumetric flexural response of the panel, which, at frequencies below the critical frequency, is the most effective sound radiating component. This is indeed a very appealing solution, although the study presented in Ref. [27], has shown that, even if the sensor and actuator transducers are spatially matched, they are not dual and collocated since their coupling via out-of-plane flexural vibration of the panel is out-of-phase with their coupling via in-plane extensional and shear vibration of the panel. Once more, this problem greatly limits the stability of the control system and therefore its performance. Nevertheless, this solution may work well on the lightweight honeycomb thick structures developed recently, where the thickness of the core structure would enhance the coupling via bending vibration and thus reduce the unwanted in-plane coupling effect too. Alternatively, Ref. [139], proposed a solution with double transducer layers bonded on the opposite faces of the panel for both the sensor and the actuator. In this way, a signal proportional to the flexural response only can be detected by taking the difference of the signals from the two transducers. Alternatively, the panel can be excited in bending only by driving out-of-phase the two transducers.

## 5. Vibration and sound transmission active control effects

The vibration and sound transmission control effects generated by the smart panels with the feed-forward and feedback active systems depicted in Table 2–5 are now analyzed in details. The control performances are assessed with respect to the spectra of the flexural kinetic energy and sound transmission ratio comprised between 0 and 2 kHz. Before discussing the effects produced by the control systems, the passive flexural response and sound transmission are first analyzed here. For instance, the black solid line in plot (a) of Figure 8 shows that, the spectrum of the panel flexural response due to the primary acoustic plane wave is characterized by well separated sharp resonance peaks up to about 800 Hz, which are due to the resonant responses of the low order flexural modes of the panel. At



**Figure 9.** Flexural kinetic energy (a) and sound transmission ratio (b) for the smart panels with the feed-forward control systems Type (c) (purple dashed lines) and Type (d) (blue dash-dotted lines) shown in Table 2.

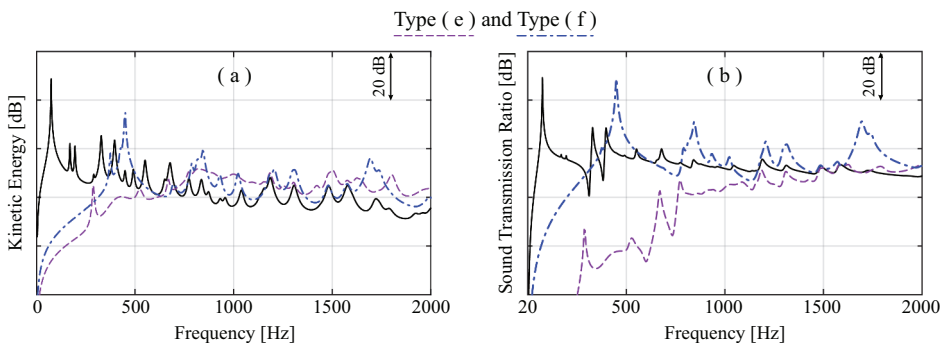
higher frequencies the spectrum is characterized by smoother crests and troughs, which are due to the overlap of the resonant responses of clusters of higher order flexural modes of the panel [6,23]. In parallel, the black solid line in plot (b) of Figure 8 shows that, up to about 800 Hz, the spectrum of the sound transmission ratio is also characterized by well separated sharp peaks, which, however, are due to the resonant responses of the volumetric flexural modes only. This is because, as shown in Figure 3, at frequencies below the critical frequency, the volumetric modes characterized by odd mode numbers are the most efficient sound radiators [6]. For example, the (1,1) mode is a much more efficient sound radiator than the modes (1,2) and (2,1). As a result, the spectrum of the sound transmission ratio shows a distinctive peak at the first resonance frequency for the (1,1) mode and nearly no peaks at the second and third resonance frequencies for the (1,2) and (2,1) modes. Above 800 Hz, the spectrum of the sound transmission ratio is also characterized by smoother crests and troughs, which are generated by the overlap of the resonant responses of clusters of higher order flexural modes of the panel [6]. Unlike the spectrum of the flexural kinetic energy, at low frequencies, the spectrum of the sound transmission ratio is characterized by sharp troughs, which are due to the sound cancellation mechanism generated by the interaction of pair of modes described in Section 3.1 [6].

### 5.1 Feed-forward control systems

The vibration and sound transmission control effects produced by the feed-forward control systems depicted in Tables 2 and 3 are first examined in this sub-section.

#### 5.1.1 Multi-channel feed-forward control systems

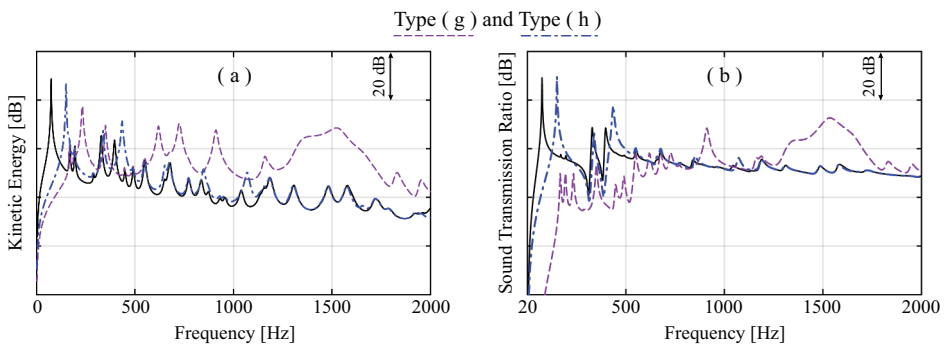
To start with, the 6 multi-channel feed-forward control systems Type (a)–(f) are considered. Figure 8 shows the spectra of the flexural kinetic energy and sound transmission ratio of the smart panels Type (a) and (b), which are equipped with the  $4 \times 4$  array of square piezoelectric patches. The purple dashed lines indicate that, when this sixteen channels system is set to minimize the sound pressure measured by the array of five microphones (Type a), there is a large reduction of the sound transmission up to about 1.2 kHz and then, at higher frequencies there is instead about 5 dB increase of the sound



**Figure 10.** Flexural kinetic energy (a) and sound transmission ratio (b) for the smart panels with the feed-forward control systems Type (e) (purple dashed lines) and Type (f) (blue dash-dotted lines) shown in Table 2.

transmission. This is due to the fact that the sound radiation is estimated by only five microphones, and thus, at higher frequencies where the acoustic wavelength becomes smaller than the distances between the microphones, the system does not produce anymore a global reduction of the sound radiation but rather a local control effect at the error microphone positions. The flexural vibration of the panel is attenuated only at low frequencies below about 420 Hz and then, at higher frequencies, there is a large increment of the flexural response. This is due to the fact that, below 420 Hz, the flexural vibration of the panel is characterized by a low modal overlap factor [6,16]. In other words, at each frequency the vibration is controlled by the resonant response of a specific low order flexural mode of the panel. Therefore, to mitigate the low frequency sound transmission, the feed-forward system should simply control the response of the low order flexural modes. In contrast, above 420 Hz, the modal overlap factor becomes progressively larger and greater than 1. Therefore, at each frequency the vibration of the panel is given by the resonant responses of multiple higher order flexural modes. However, the 16-channels feed-forward system cannot effectively control the responses of these clusters of modes. Hence, it rearranges the amplitudes of the resonant responses of these modes in such a way as to maximize the sound cancellation effect that arises from their mutual radiations [61,62]. This results in the increment of the panel flexural vibration above 420 Hz [97], which however effectively reduces the sound transmission up to about 1.2 kHz [21]. At higher frequencies this sound cancellation mechanism still works, but only to produce a local control effect at the error microphone positions. Thus, there is no reduction of the sound transmission through the panel.

The blue dash-dotted lines in the two plots of Figure 8 indicate that, when the  $4 \times 4$  array of piezoelectric patches are driven to minimize the velocities measured by the 16 MST accelerometers located at the centers of the piezoelectric patches, both the flexural kinetic energy spectrum and sound transmission ratio spectrum maintain similar levels than those of the panel with no control. The two spectra show a clear shift to higher frequencies of the resonance peaks. This is because the control system drives the 16 control patches to minimize the vibrations at their centers where the error sensors are located. In this way, the response of the panel can be assimilated to that of a stiffer simply supported panel, which is constrained at the  $4 \times 4$  array of error sensor positions. The new

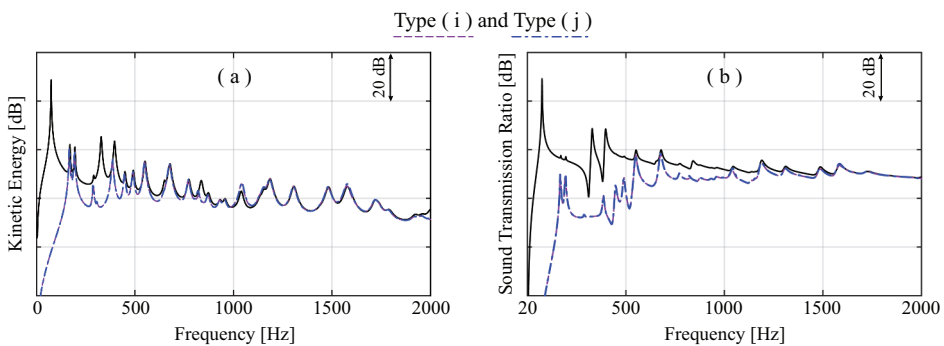


**Figure 11.** Flexural kinetic energy (a) and sound transmission ratio (b) for the smart panels with the feed-forward control systems Type (g) (purple dashed lines) and Type (h) (blue dash-dotted lines) shown in Table 3.



flexural modes will be characterized by ‘quilted’ shapes, which actually radiate sound more efficiently [28], as it happens with periodic structures for example [6]. Moreover, the natural frequencies of these new modes will be comparatively higher. Therefore, the spectra of the flexural kinetic energy and sound transmission ratio show a shift to higher frequencies of the resonance peaks. Also, the spectrum of the sound transmission ratio show little increments of the amplitudes of the resonance peaks, which are due to the fact that the new modes have higher sound radiation efficiencies. In summary, the results presented in Figure 8 suggest that the  $4 \times 4$  array of piezoelectric patches can be effectively used to control the sound transmission produced by an incident sound field, provided the feed-forward controller is set to minimize the sound radiation. This is not a simple task since it requires an array of microphones specifically tailored to detect the sound radiated by the panel. Nevertheless, a controller set to minimize the flexural vibration at a grid of points would not work either, since it modifies the flexural response of the panel in such a way it radiates sound more efficiently.

The plots in Figure 9 show the spectra of the flexural kinetic energy and sound transmission ratio of the smart panels Type (c) and (d), which are equipped with the array of 16 isosceles triangular piezoelectric patches having the base edges evenly distributed along the four edges of the panel. The purple dashed lines indicate that, when this sixteen channels system is set to minimize the sound pressure measured by the array of five microphones (Type c), there is a significant reduction of the sound transmission up to 1.2 kHz. Instead, the flexural response is attenuated only at low frequencies below 500 Hz. Comparing the purple-dashed lines in Figures 8 and 9, it can be noticed that the systems with the  $4 \times 4$  array of square patches and with the array of 16 triangular patches produce similar effects. This is because the triangular actuators were designed to have quite a large height such that the transverse forces generated at the vertices of the patches effectively couple with the low order modes of the panel. The purple dashed line in Plot (a) of Figure 9, shows that, also this arrangement controls the flexural response only at low frequencies below about 500 Hz. Instead, at higher frequencies there is a significant control spillover effect, which is due to the reconstruction of the panel modal response to minimize the sound pressure at the error sensors. As seen for the panel with square piezoelectric patches, this results into a global reduction of the sound



**Figure 12.** Flexural kinetic energy (a) and sound transmission ratio (b) for the smart panels with the feed-forward control systems Type (i) (purple dashed lines) and Type (j) (blue dash-dotted lines) shown in Table 3.

transmission only up to about 1.2 kHz, since, at higher frequencies, the distances between the microphone error sensors are greater than the acoustic wavelength. The blue dash-dotted lines in the two plots of Figure 9 indicate that, when the 16 triangular piezoelectric patches are driven to minimize the velocities measured by the 16 MST accelerometers located at the vertices of the piezoelectric patches, there is a substantial reduction of the sound transmission up to about 1 kHz and a significant reduction of the flexural kinetic energy below 500 Hz. Again, this mismatch is due to the fact that above 500 Hz, the control system rearranges the flexural response of the panel in such a way as to maximize the sound cancellation effects between pairs of modes. Nevertheless, it is interesting to note that this control system generates quite good reductions of the sound transmission up to about 1 kHz, despite the error sensors measure panel velocities rather than sound pressure.

Figure 10 shows the spectra of the flexural kinetic energy and sound transmission ratio of the smart panels Type (e) and (f), which are equipped with the  $3 \times 3$  array of proof-mass electromagnetic force actuators. The purple dashed lines indicate that, when this nine channels system is set to minimize the sound pressure measured by the array of five microphones (Type e), the sound transmission is effectively controlled up to about 1.4 kHz, with reductions greater than 10 dB up to 1 kHz. At higher frequencies around 2 kHz there is a slight increment of the sound transmission, which, once more, is due to the fact that the sound radiation is estimated by a finite number of microphones. As seen for the panels with the piezoelectric actuators, the flexural response of the panel is attenuated only at low frequencies, whereas, above about 600 Hz, it is actually increased by 5–10 dB. Once more, the control system rearranges the amplitudes of the resonant responses of the higher order modes in such a way as to maximize the sound cancellation effect that arises from their mutual radiations. Therefore, above 600 Hz the reduction of the sound transmission is obtained at the expenses of an increment of the flexural vibration of the panel. The blue dash-dotted lines in the plots of Figure 10 suggest that, when the  $3 \times 3$  array of proof-mass electromagnetic force actuators are driven to minimize the velocities measured by the 9 MST accelerometers located at the footprints of the actuators, the spectra of the flexural kinetic energy and of the sound transmission ratio maintain similar levels than those of the panel with no control. There is a significant shift

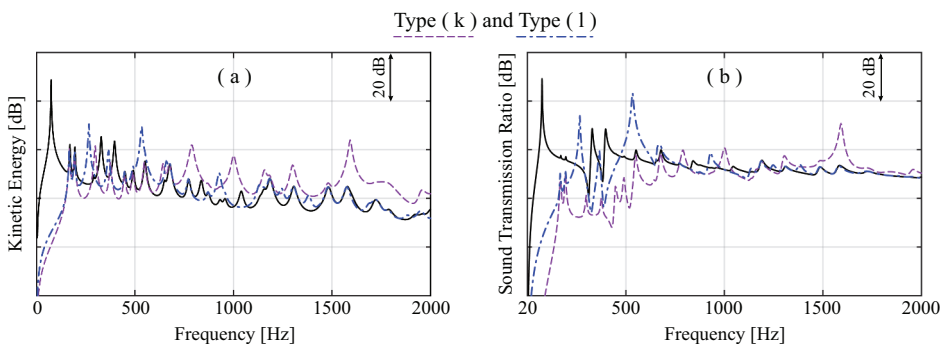


Figure 13. Flexural kinetic energy (a) and sound transmission ratio (b) for the smart panels with the feed-forward control systems Type (k) (purple dashed lines) and Type (l) (blue dash-dotted lines) shown in Table 3.

to higher frequencies of the resonance peaks, which is due to the fact that the control system effectively cancels the flexural vibrations at the 9 control positions. Therefore the flexural response of the panel can be assimilated to that of a stiffer simply supported panel pinned at the  $3 \times 3$  array of error sensor positions, which is thus characterized by 'quilted' mode shapes with higher resonance frequencies and higher sound radiation efficiency [6,28]. In conclusion, as seen for the panel with the square piezoelectric patch actuators, the  $3 \times 3$  array of proof-mass electromagnetic force actuators can be used to effectively control the sound transmission, provided the system is set to minimize the sound radiation estimated with a finite number of microphones rather than the flexural response estimated with a finite number of accelerometers.

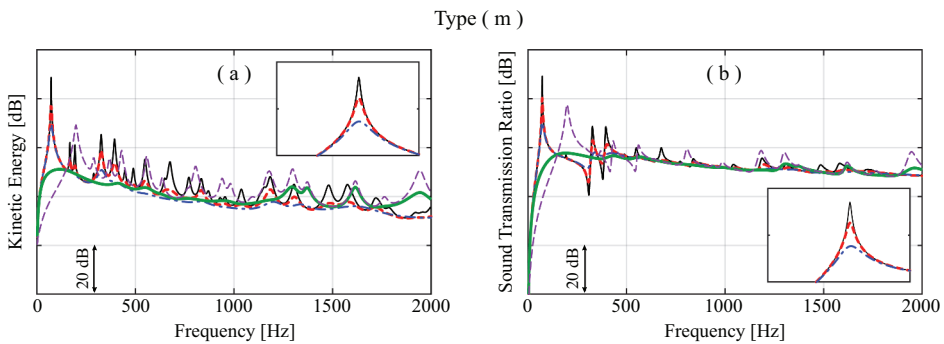
### 5.1.2 Single-channel feed-forward control systems

The single-channel feed-forward control systems Type (g)–(l) are now examined. To start with, [Figure 11](#) shows the spectra of the flexural kinetic energy and sound transmission ratio of the smart panels Type (g) and (h), which are equipped with the  $4 \times 4$  array of square piezoelectric patches. The purple dashed lines indicate that, when sixteen actuators are driven by the same control signal to minimize the sum of the sound pressures measured by the array of five microphones (Type g), there is about 20 dB reduction of the sound transmission up to about 500 Hz. However, there is also a significant increment of the sound transmission between 1.3 and 1.7 kHz, which is due to the facts that the sound radiation is estimated only with five microphones and the control actuators are driven by the same control signal. Also, the flexural vibration of the panel is attenuated only at very low frequencies below about 160 Hz. As seen for the multi-channel systems using the  $4 \times 4$  array of square piezoelectric patches, below about 160 Hz, the control of sound transmission is obtained by reducing the overall vibrational response of the panel. Instead, above 160 Hz the reduction of sound transmission is obtained by rearranging the amplitudes of the resonant responses of the low order modes in such a way as to maximize the sound cancellation effect that arises from their mutual radiations. Contrasting the purple lines in the plots of [Figures 11](#) and [8](#), it can be concluded that, although the multi-channel system clearly outperform the single-channel system, the latter yet produces at least 20 dB reduction of the sound transmission up to 500 Hz.

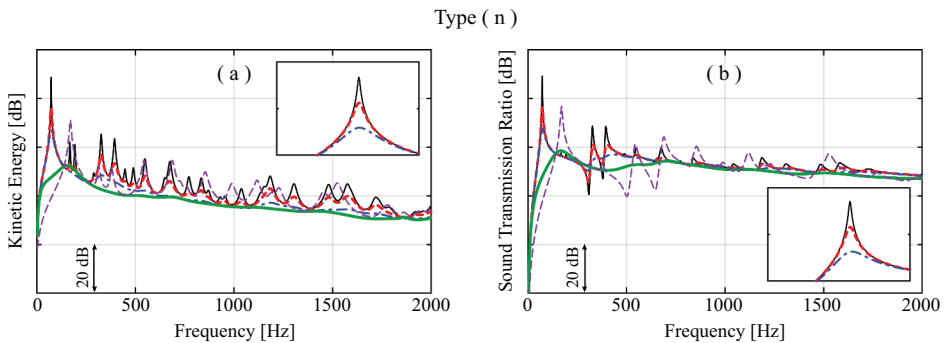
The blue dash-dotted lines in the two plots of [Figure 11](#) indicate that, when the  $4 \times 4$  array of piezoelectric patches are driven to minimize the sum of the velocities measured by the 16 MST accelerometers located at the centers of the piezoelectric patches, both the flexural kinetic energy and sound transmission ratio spectra maintain similar levels than those of the panel with no control. There is just a shift to higher frequencies of the resonance peaks. This is the result of the same phenomenon described above for the multi-channel system with the square piezoelectric patches and accelerometer sensors. Indeed, also the single-channel system drives the actuators to pin the panel at the 16 error sensor positions so that the flexural response is characterized by the 'quilted' mode shapes, which have higher sound radiation efficiencies.

[Figure 12](#) shows the spectra of the flexural kinetic energy and sound transmission ratio of the smart panels Type(i) and (j), which are equipped with a distributed piezoelectric film actuator having quadratically shaded electrodes. As shown in [Section 4.3.3](#), this distributed actuator generates lines of flexural excitations, which can be assimilated to a uniform transverse force excitation. Therefore, the bending

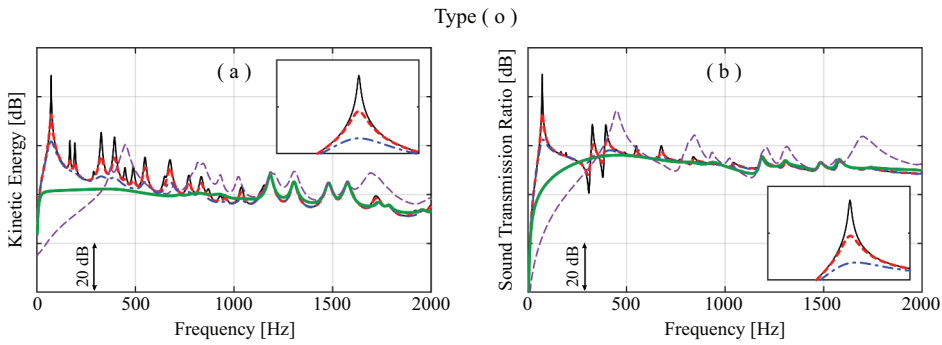
excitation field produced by this actuator is well coupled with the first radiation mode of the plate, which, as discussed in Section 3.1, is the most efficient sound radiator at frequencies below the critical frequency [6]. Indeed, the purple-dashed lines show that, when this actuator is driven to minimize the sum of the sound pressure measured by the array of five microphones (Type i), there is a 20 dB reduction of the sound transmission up to about 500 Hz, apart from the resonance frequencies at about 167 and 193 Hz. Also, there is a 6 dB reduction between 500 and 900 Hz. The purple dashed line in Plot (a) of Figure 12 shows that, this system effectively controls the resonant responses of the low order flexural modes of the panel, which are characterized by odd mode orders, that is by volumetric displacements. Instead, it has very little effect on the resonant responses of the modes with one or both even mode numbers, such as for example the (2,1) and (1,2) modes, which resonate at about 167 and 193 Hz. These modes do not show a net volumetric displacement and thus couple poorly with the uniform force actuator so that the feed-forward system produces little vibration and sound transmission control effects at their resonance frequencies. Nevertheless, these modes are characterized by poor



**Figure 14.** Flexural kinetic energy (a) and sound transmission ratio (b) for the smart panel Type (m) – Table 4, which implements low gains (red dotted lines), medium gains (blue dash-dotted lines), optimal gains (green solid lines), very large control gains (purple dashed lines).

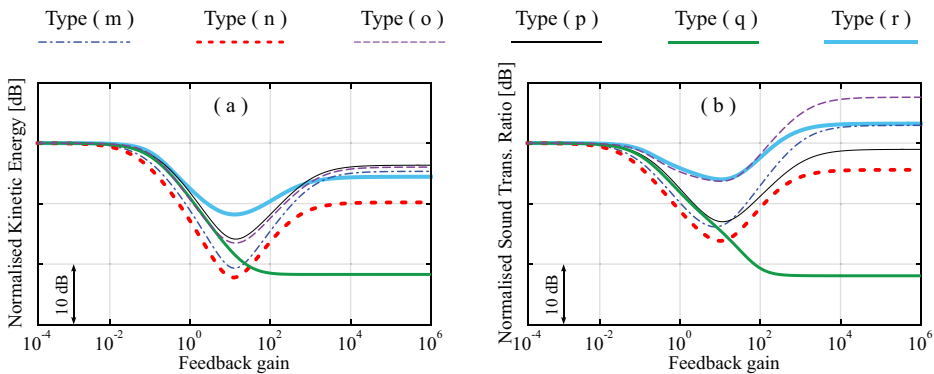


**Figure 15.** Flexural kinetic energy (a) and sound transmission ratio (b) for the smart panel Type (n) – Table 4, which implements low gains (red dotted lines), medium gains (blue dash-dotted lines), optimal gains (green solid lines), very large control gains (purple dashed lines).



**Figure 16.** Flexural kinetic energy (a) and sound transmission ratio (b) for the smart panel Type (o) – Table 4, which implements low gains (red dotted lines), medium gains (blue dash-dotted lines), optimal gains (green solid lines), very large control gains (purple dashed lines).

sound radiation too such that, as can be noticed in Plot (b), the sound transmission at the 167 and 193 Hz is low in any case. In conclusion, this system effectively controls the sound transmission up to about 1 kHz without increasing the flexural response of the panel, that is without control spillover effect. The blue dash-dotted lines in the two plots of Figure 12 show the control effects produced when the distributed piezoelectric film actuator with quadratically shaped electrodes is driven to minimize the volume velocity vibration field estimated with a matched distributed piezoelectric film sensor (system Type j). The two spectra suggest that this system generates very similar vibration and sound transmission control effects than those obtained with the system Type (i), which is set to minimize the sum of the sound pressure measured by the array of five microphones. Indeed the smart panel reduces the sound transmission by 20 dB, up to about 500 Hz, and then by 6 dB up to 900 Hz. This result is produced by controlling the resonant response of the volumetric modes characterized by odd mode numbers, which are the most effective sound radiators and are effectively detected and excited by the matched distributed sensor–actuator pair. This system offers a very interesting practical solution, where



**Figure 17.** Frequency averaged flexural kinetic energy (a) and sound transmission ratio (b) against the control gains in the feedback loops of the smart panels Type (m) – (r).

the sensor and actuator are embedded on the panel to form a compact smart structure, which is driven by a simple single channel feed-forward controller.

Figure 13 shows the flexural kinetic energy and sound transmission ratio of the smart panels Type (k) and (l), which are equipped with the  $3 \times 3$  array of proof-mass electromagnetic force actuators. The purple dashed lines show that, when the nine actuators are driven by the same control signal to minimize the sum of the sound pressure measured by the array of 5 microphones (Type k), there is about 20 dB reduction of the sound transmission up to about 500 Hz. At higher frequencies, the level of the sound transmission remains unaltered, apart from a very large new resonance peak at about 1.6 kHz, which is due to two concurrent facts. Firstly, the uniform force actuator is discretized with an array of 9 point force actuators. Secondly, the sound radiation sensor is discretized with an array of 5 point microphone sensors. Consequently, as shown by the purple dashed line in Plot (a), this system effectively cancels the resonant response of the fundamental (1,1) mode only. Indeed, above about 80 Hz, the spectrum of the flexural kinetic energy maintains a similar or higher level than that for no control (black solid line). Once more, this is because, to minimize the sum of the 5 error sound pressures, the 9 force actuators tend to rearrange the modal response of the panel in such a way as to maximize the sound radiation cancellation effect produced by pairs of modes. Nevertheless, this control mechanism works well up to 500 Hz only. As discussed above for the single-channel system with square piezoelectric patch actuators, this is because, at higher frequencies, the sum of the five microphone sensors does not provide an accurate estimate of the sound radiation and the nine control actuators driven by the same control signal cannot rearrange properly the modal response of the panel. To conclude, the blue dash-dotted lines in the two plots in Figure 13 show the control effects produced when the  $3 \times 3$  array of proof-mass electromagnetic force actuators are driven by the same control signal to cancel the sum of the velocities measured by the  $3 \times 3$  array of MST accelerometers located at the footprints of the actuators. Plot (b) shows that there is actually no control effect of the sound transmission apart from very low frequencies below 240 Hz. Plot (a) shows that the control systems effectively cancels the resonant response of the first mode only. This is because the system minimizes an estimate of the volumetric component of the flexural vibration of the panel obtained from the sum of the nine error velocities using a discretized uniform force excitation given by the nine point forces driven in phase. As a result, there is quite a marked vibration and sound transmission control spillover effect at higher frequencies, which give rise to the typical flexural response composed by 'quilted' mode shapes.

### 5.1.3 Summary on feed-forward control systems

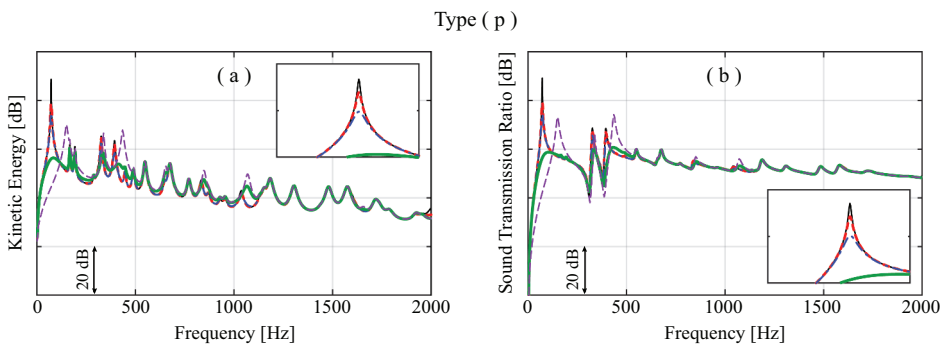
The results presented in the previous two sub-sections have shown that, in general, the multi-channel feedforward control systems outperform the single channel systems, although, the system formed by the matched volume velocity sensor and uniform force actuator has given very interesting results, with comparable reductions of the sound transmission. Moreover, this system is not affected by the higher frequencies vibration control spillover phenomenon that arises from both the modal reconstruction mechanism typical of multi-channel control systems and the sensing-actuation discretization typical of single-channel systems using point actuators and point sensors.

## 5.2 Feedback control systems

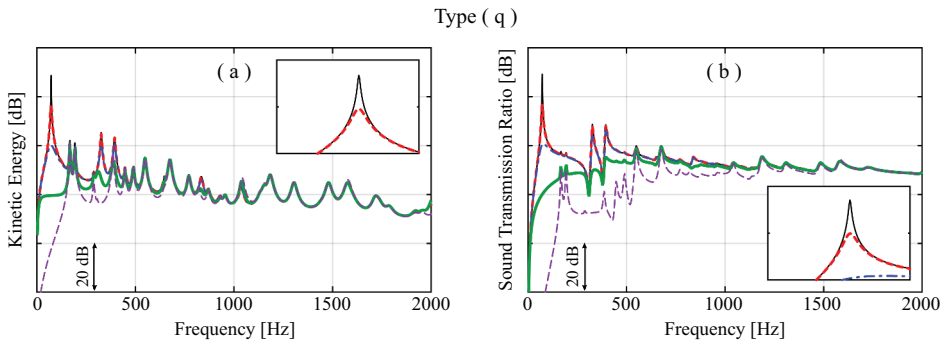
The vibration and sound transmission control effects produced by the multi- and single-channel feedback control systems depicted respectively in Tables 4 and 5 are now considered.

### 5.2.1 Multi-channel feedback control systems

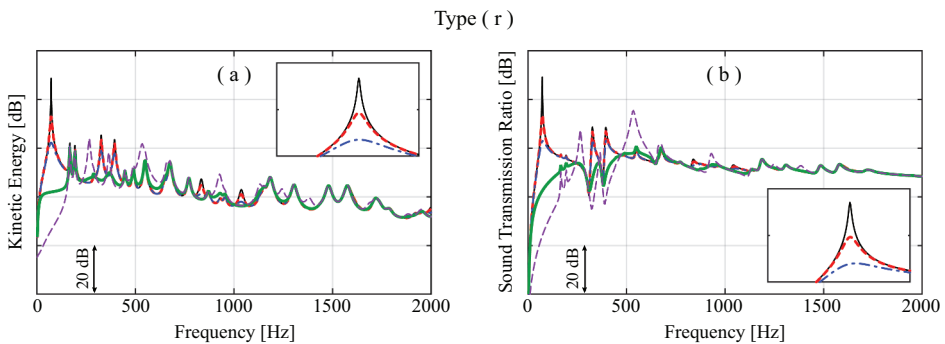
First, the multi-channel feedback control systems Type (m), (n), and (o) are examined considering the spectra of the flexural kinetic energy and sound transmission ratio shown in Figure 14, 15, 16. To start with, Figure 14 shows the flexural kinetic energy and sound transmission ratio of the smart panel Type (m), which is equipped with a  $4 \times 4$  array of decentralized velocity feedback loops using square piezoelectric patch actuators with, at their centers, miniaturized MST accelerometer sensors. The red dotted and blue dash-dotted lines in the two plots show that the amplitudes of the resonance peaks in the two spectra are progressively attenuated as the control gains are raised. This is the result of the active damping produced by the velocity feedback control loops, which effectively reduce the panel vibration, and thus its sound transmission, around resonance frequencies [6]. However, the purple dashed lines, show that, when very large larger feedback gains are implemented, the two spectra develop new sharp resonance peaks at comparatively higher frequencies than those of the panel with no control. This phenomenon is due to the same pinning effect discussed above for the feed-forward control system set to minimize the velocities measured by the accelerometer error sensors at the centers of the square piezoelectric patches [140]. Indeed, when very large feedback gains are implemented, each feedback loop tends to cancel the error velocity signal measured by the accelerometer sensors positioned at the center of the square piezoelectric patch actuators. As a result, the feedback control units do not produce anymore the active damping necessary to reduce the resonant responses of the flexural modes. On the contrary, they generate a  $4 \times 4$  array of pinning points such that the response of the panel is given by new flexural modes with ‘quilted’ shapes, which resonate at comparatively higher frequencies than the modes of the panel with no control [28]. The overall reduction of the flexural response and sound transmission is exemplified in Figure 17,



**Figure 18.** Flexural kinetic energy (a) and sound transmission ratio (b) for the smart panel Type (p) – Table 5, which implements low gain (red dotted lines), medium gain (blue dash-dotted lines), optimal gain (green solid lines), very large control gain (purple dashed lines).



**Figure 19.** Flexural kinetic energy (a) and sound transmission ratio (b) for the smart panel Type (q) – Table 5, which implements low gain (red dotted lines), medium gain (blue dash-dotted lines), optimal gain (green solid lines), very large control gain (purple dashed lines).



**Figure 20.** Flexural kinetic energy (a) and sound transmission ratio (b) for the smart panel Type (r) – Table 5, which implements low gain (red dotted lines), medium gain (blue dash-dotted lines), optimal gain (green solid lines), very large control gain (purple dashed lines).

which shows the flexural kinetic energy and sound transmission ratio averaged between 0 Hz and 2 kHz with respect to the control gains implemented in the feedback loops. The blue dash-dotted lines in the two plots show that both the frequency-averaged flexural response and the frequency-averaged sound transmission tend to decrease as the feedback gains are raised and reach their minima for feedback gains of about 10. Overall, the frequency-averaged flexural response is brought down by about 21 dB whereas the frequency-averaged sound transmission is reduced by 13 dB. The green thick solid lines in Figure 14 show the spectra of the flexural kinetic and sound transmission ratio when the optimal feedback gain is implemented in the 16 feedback loops. If the 16 control gains were further increased, these control effects would vanish and eventually the frequency-averaged flexural response would settle around 5 dB whereas the frequency-averaged sound transmission would actually become 3 dB greater than that of the panel with no control. This is the result of the pinning effect that generates ‘quilted’ flexural mode shapes, which radiate sound more efficiently than the mode shapes of the plain panel [29,140].



Figure 15 shows the flexural kinetic energy and sound transmission ratio of the smart panel Type (n), which is equipped with an array of 16 decentralized velocity feedback loops using the triangular piezoelectric patch actuators with the base edges evenly scattered over the perimeter of the panel and miniaturized MST accelerometer sensors located at the tips of the patches. As found for the system with the square piezoelectric patch actuators, the active damping produced by the velocity feedback control loops effectively reduce the panel vibration, and thus its sound transmission, around resonance frequencies [6]. Indeed, the red dotted and blue dash-dotted lines in the two plots show that, as the control gains are raised, the amplitudes of the resonance peaks in the two spectra are progressively attenuated. Nevertheless, the purple dashed lines show that, also in this case, for very large control gains, the two spectra show again sharp resonance peaks.

Once more, with high control gains, the feedback loops tend to pin the panel at the error sensor positions, that is at the vertices of the triangular piezoelectric patch actuators. Therefore, no active damping is generated on the panel and, accordingly, the spectra of the flexural kinetic energy and sound transmission ratio show sharp resonance peaks, which are shifted to higher frequencies. In this case, the sixteen pinning points form a new rectangular boundary edge, which, in a way, reduces the vibrating surface of the panel so that the flexural mode shapes are characterized by higher natural frequencies and thus higher resonance frequencies [28]. The red dotted line in the two plots of Figure 17 confirm that both the frequency-averaged flexural response and the frequency-averaged sound transmission tend to decrease as the feedback gains are raised and reach their minima for feedback gains of about 10. In this case, overall, the frequency-averaged flexural response is brought down by about 22 dB whereas the frequency-averaged sound transmission is reduced by 16 dB. Therefore, when the optimal feedback gain is implemented in the 16 feedback loops, the flexural kinetic energy and sound transmission ratio show the smoothed spectra depicted by the green thick solid lines in the two plots of Figure 15. When the control gains are further increased, the pinning phenomenon attenuates these control effects. Indeed, for very large control gains, the frequency-averaged flexural response and the frequency-averaged sound transmission are reduced by 10 dB and 4 dB respectively. In this case, the pinning effect reduces the size of the vibrating surface and thus does not increase the sound radiation efficiency of the natural modes [28].

Figure 16 shows the spectra for the flexural kinetic energy and sound transmission ratio of the smart panel Type (o), which is equipped with a  $3 \times 3$  array of decentralized velocity feedback loops using proof-mass electromagnetic actuators with miniaturized MST accelerometer sensors at their footprints. The red dotted and blue dash-dotted lines in the two plots show that, as the control gains are brought up, the amplitudes of the resonance peaks in the two spectra are progressively attenuated by the active damping produced by the velocity feedback control loops [6]. Nevertheless, as noticed for the panel Type (m), the purple-dashed lines, shows that, when very large larger feedback gains are implemented, the two spectra develop new sharp resonance peaks at higher frequencies than those of the panel with no control. In this case too, for very large control gains, the feedback loops drive to zero the vibrations at the control positions. This results into a  $3 \times 3$  array of pinning points such that the flexural response of the panel is characterize by 'quilted' mode shapes, which resonate at higher frequencies than the modes of the plain

panel [30,34,40,140]. The green thick solid lines in the two plots of Figure 16 show that, when the optimal feedback gains are implemented, the resonance peaks of the flexural response and sound transmission spectra are effectively smoothed at frequencies below 1 kHz. Accordingly, as can be noticed from the purple dashed lines in Figure 17, the frequency-averaged flexural response and sound transmission are reduced by 17 and 6 dB respectively. Instead, for very large control gains such that the pinning effect takes place, the frequency-averaged flexural response is reduced by 4 dB and the frequency-averaged sound transmission is increased by 8 dB. As seen for the panel Type (m), this is due to the fact that the quilted flexural vibration of the panel generated by high feedback gains radiates sound more effectively than a plain panel [6].

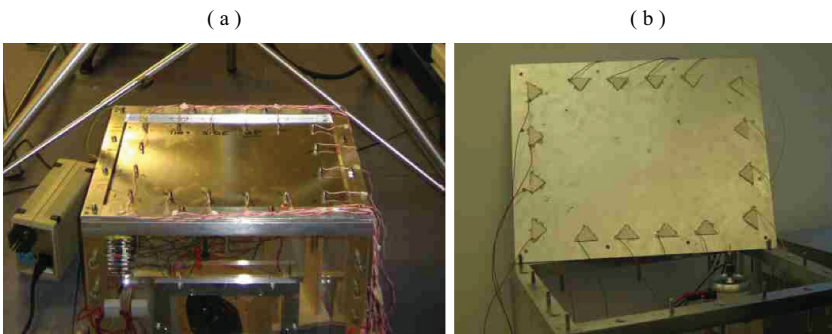
### 5.2.2 Single-channel feedback control systems

The single-channel feedback control systems Type (p), (q), (r) are now examined with respect to the spectra of the flexural kinetic energy and sound transmission ratio shown in Figure 18, 19, 20. To start with, Figure 18 shows the two spectra for the smart panel Type (p), which is equipped with a  $4 \times 4$  array of square piezoelectric patch actuators having miniaturized MST accelerometer sensors at their centers. The output velocity signals from the error sensors are summed into a single velocity signal, which is inverted and amplified, and then feedback to the actuators. The red dotted and blue dash-dotted lines in the two plots show that, for moderate feedback control gains, this system produces only minor control effects, which are restricted to the first resonance peak. This is because the combined signal from the 16 sensors gives an estimate of the volumetric flexural vibration of the panel. Moreover, the flexural excitation field produced by the 16 actuators approximates a uniform flexural excitation over the panel. Therefore, the single channel feedback system works on the resonant responses of volumetric flexural modes, that is those with both even mode numbers. The  $4 \times 4$  array of point sensors gives only a rough estimate of the volumetric vibration of the panel. Similarly, the  $4 \times 4$  array of square piezoelectric patch actuators generate only a coarse uniform flexural excitation over the panel surface. Therefore, the feedback loop effectively works only on the resonant response of the first (1,1) flexural mode. As found with the decentralized control systems discussed above, for very large feedback gains, the system tends to pin the flexural vibration of the panel at the 16 sensor positions such that the spectra of the flexural kinetic energy and sound transmission ratio show similar levels as those with no control, but with resonance peaks shifted to higher frequencies. The black solid lines in Figure 17 show that, when the optimal feedback gain of about 10 is implemented, the flexural response and sound transmission averaged between 0 Hz and 2 kHz are brought down by about 15 and 13 dB respectively. Nevertheless, as shown by the green solid lines in the two plots of Figure 18, this reduction is due primarily to the cancellation of the first resonance peak at about 72 Hz, which is linked to the resonant response of the first flexural mode of the panel.

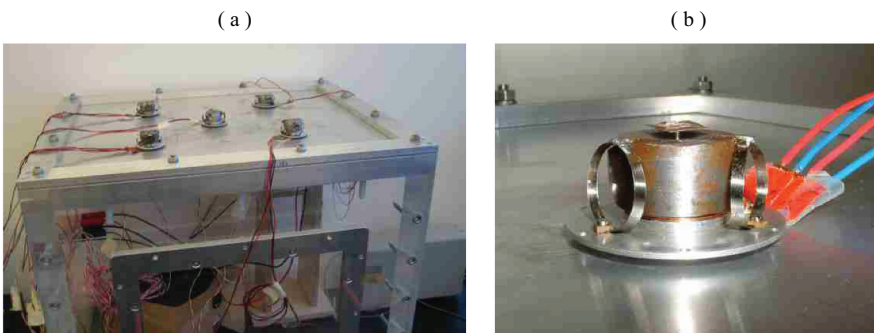
Figure 19 shows the spectra of the flexural kinetic energy and sound transmission ratio of the smart panel Type (q), which is composed by a matched volume velocity sensor and a uniform force actuator made with piezoelectric foils having quadratically shaped electrodes bonded on either side of the panel. The four lines in the two plots show that, as the control gains are raised, the amplitudes of the peaks generated by resonant responses of the panel flexural modes with even mode numbers are progressively reduced. Indeed, the green solid lines in Figure 17 show that, as the feedback control



**Figure 21.** Prototype smart panel with a  $4 \times 4$  array of decentralized velocity feedback loops formed by square piezoelectric patch actuators with accelerometer sensors at their centers [33].

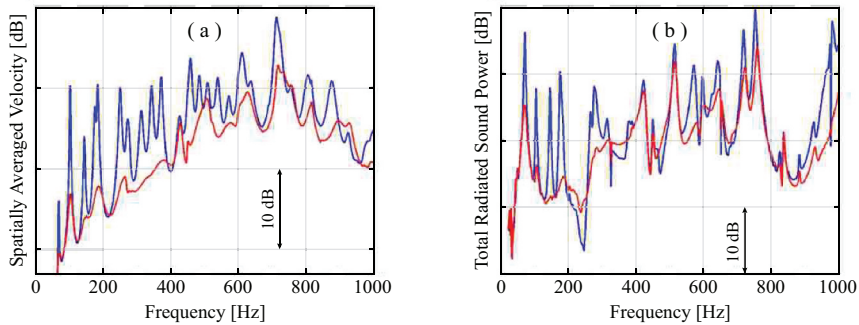


**Figure 22.** Prototype smart panel with 16 decentralized velocity feedback loops formed by triangular piezoelectric patch actuators with accelerometer sensors at their tips [35].

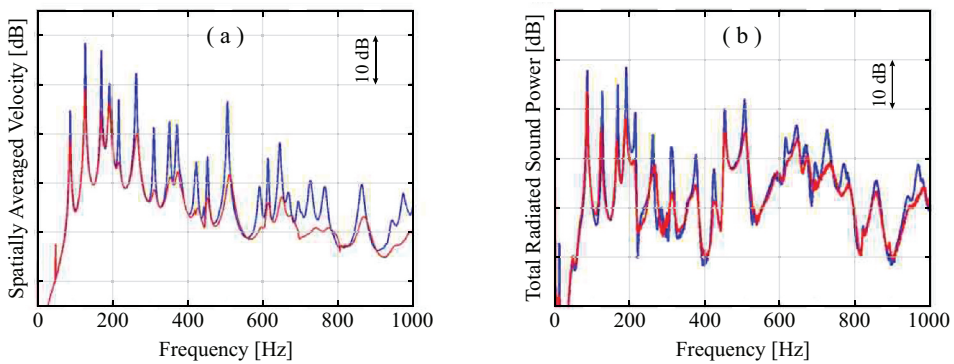


**Figure 23.** Prototype smart panel with 5 decentralized velocity feedback loops formed by electromagnetic proof-mass force actuators with accelerometer sensors at their footprints [34].

gain is increased, the 0 Hz – 2 kHz frequency-averaged flexural kinetic energy and sound transmission ratio monotonically fall down toward a minimum value. For instance, for control gains greater than 250, both the frequency averaged flexural kinetic energy and

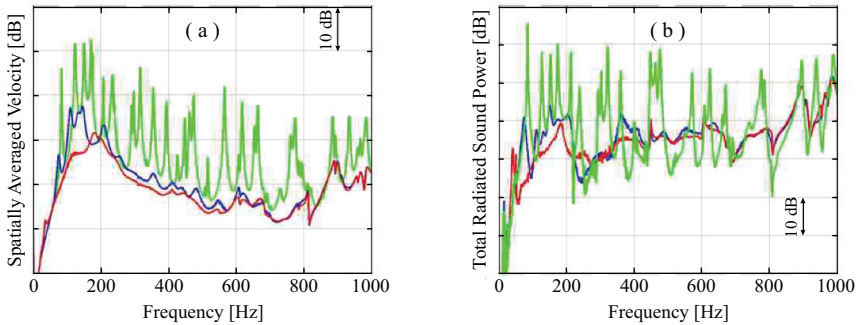


**Figure 24.** Measured spectra of the spatially averaged velocity (a) and sound radiated power (b) of the smart panel shown in Figure 21, without control (solid blue lines) and with control (solid red lines) [33].



**Figure 25.** Measured spectra of the spatially averaged velocity (a) and sound radiated power (b) of the smart panel shown in Figure 22, without control (solid blue lines) and with control (solid red lines) [35].

the frequency averaged sound transmission ratio are reduced by about 22 dB. As can be noticed from the colored lines in Plot (a) of Figure 19, the feedback loop with matched volume velocity sensor and uniform force actuator pair effectively control the resonant responses of the volumetric modes of the panel, which are characterized by odd mode numbers. As discussed in Section 3.1, below the critical frequency [6], the volumetric modes are actually the most efficient sound radiators. Therefore, the volume velocity and uniform force matched sensor-actuator pair is very effective in reducing the sound transmission through the panel, without generating the undesired pinning effect for high control gains. In principle, a feedback loop with a matched sensor-actuator pair should be unconditionally stable [58], so that the large feedback gains necessary to achieve large reductions of the flexural vibration and sound transmission shown by the green thick solid lines in the two plots of Figure 17 can be implemented in practice. However, the study presented in Ref. [27], showed that this would be true if the two transducers were coupled only via flexural vibrations. As discussed in Section 3, they are instead coupled both via in-plane extensional and shear vibrations and via out-of-plane flexural vibrations. The two coupling effects are out of phase and thus, as shown in Ref.



**Figure 26.** Measured spectra of the spatially averaged velocity (a) and sound radiated power (b) of the smart panel shown in Figure 23, without actuators (solid green lines) with open loop actuators (solid blue lines) and with closed loop actuators (solid red lines) [34].

[27], the feedback loop is characterized by limited stability properties. The extent of this problem strongly depends on the design of the panel. For instance, thick panels, such as for example honeycomb panels, will be characterized by a stronger coupling of the two transducers via out-of-plane flexural vibration. Alternatively, transducers formed by double layers connected in counter-phase could be used to detect and generate only flexural vibrations [139].

To conclude, Figure 20 shows the flexural kinetic energy and sound transmission ratio of the smart panel Type (r), which is equipped with a  $3 \times 3$  array of proof-mass electromagnetic force actuators with at their footprints miniaturized MST accelerometer sensors. The output velocity signals from the error sensors are summed into a single velocity signal, which is inverted and amplified, and then feedback to the actuators. Similarly to panel Type (p) with the square piezoelectric patch actuators, as the feedback control gain is raised, this system produces only minor control effects, which are limited to the first resonance peak in the spectra of the flexural kinetic energy and sound transmission ratio. In this case too, the 9 sensors coarsely estimate the volumetric flexural vibration of the panel and the 9 actuators roughly approximate a uniform flexural excitation over the panel. Therefore, the single channel feedback system works quite well on the resonant responses of first (1,1) mode, but doesn't produce relevant effects on the resonant responses of both the higher order volumetric modes characterized by odd mode numbers and the modes characterized by one or both even numbers. As seen above for panel Type (p), for very large feedback gains, the system tends to pin the flexural vibration of the panel at the nine sensor positions such that the spectra of the flexural kinetic energy and sound transmission ratio show similar levels as with no control but with resonance peaks shifted to higher frequencies. As a result, the cyan solid lines in the two plots of Figure 17 show that, when the optimal feedback gain of about 10 is implemented, the frequency-averaged flexural response and sound transmission are brought down only by about 12 and 6 dB respectively. The green solid lines in the two plots of Figure 20, suggest that these reductions are due primarily to the cancellation of the first resonance peak at about 72 Hz, which is linked to the resonant response of the first flexural mode of the panel with mode numbers (1,1). For very higher control gains,

the frequency-averaged flexural response is lowered by 6 dB whereas the frequency-averaged sound transmission is raised by 3 dB.

### 5.2.3 Summary on feedback control systems

The results presented in this section have shown that, in general, the multi-channel feedback control systems outperform the single channel systems. This is the case particularly for the systems with the  $4 \times 4$  array of piezoelectric patch actuators or the system with the 16 triangular piezoelectric patch actuators. Instead, the system with the  $3 \times 3$  array of proof-mass actuators does not generate the same levels of control. This is partially because this system is composed by 9 control units only, whereas the other two encompass 16 units. Nevertheless, this disparity arises from the fact that the proof-mass electromagnetic actuators are heavier and occupies more space. Therefore, to have a realistic smart structure, comparatively fewer units are used than for the panels with the piezoelectric patches. In this respect, it is important to emphasize that this study assumed all feedback loops could implement the control gains necessary to generate the desired control action. In practice, every type of feedback loop has intrinsic limitations due to both stability of the feedback loop and saturation effects of the actuators, which therefore may not be able to deliver the required control action. As already noticed for the feed-forward control systems, the single channel systems set to control the volumetric component of the flexural vibration using a matched volume velocity sensor and uniform force actuator made from large piezoelectric foils with quadratically shaped electrodes of the panel generate significant reductions of the sound transmission at low frequencies below 500 Hz.

## 6. Prototype panels

Figure 21–23 show three prototype smart panels, which were studied in Refs. [33–35]. The panel shown in Figure 21 is composed by  $4 \times 4$  array of decentralized velocity feedback loops using square piezoelectric patch actuators with at their centers small accelerometer sensors. The panel depicted in Figure 22 is also characterized by 16 velocity feedback loops, which are made by triangularly shaped piezoelectric actuators, with their base edges evenly scattered over the perimeter of the panel, and small accelerometer sensors at their tips. Finally, the panel shown in Figure 23 encompasses five velocity feedback loops formed by a proof-mass electromagnetic force actuator with at its footprint an accelerometer sensor.

Plots (a) in Figure 24–26 show the 0–1 kHz spectra of the spatially averaged flexural vibration of the three panels measured with a laser vibrometer. Also, Plots (b) show the 0–1 kHz spectra of total sound power radiated by the three panels measured in an anechoic chamber with a standard setup composed by 9 microphones. The panel with  $4 \times 4$  array of square piezoelectric patches produces quite a large reduction of the flexural response over the whole frequency range. More specifically, it generates 10 to 20 dB reductions of the resonance peaks in the 0–1 kHz frequency range. Also, it effectively controls the sound radiation, with reductions of the resonance peaks in the 0–1 kHz frequency range comprised between 5 and 15 dB. The panel with the 16 triangular piezoelectric patches is slightly less effective. Nevertheless, it generates between 5 to 15 dB reductions of the flexural vibration resonance peaks in the 0–1 kHz frequency band.

Also, it reduces by 5 to 10 dB the sound radiation resonance peaks comprised between 0 and 1 kHz. Finally, the panel with the 5 proof-mass electromagnetic force actuators is characterized by quite significant passive control effects. Indeed, contrasting the green lines for the plain panel with the blue lines for the panel with the open loop proof-mass electromagnetic actuators, it can be noted that all resonance peaks in the 0 Hz – 1 kHz frequency band are effectively smoothed. Thus, the response and sound radiation at resonance frequencies is lowered by 10 to 15 dB. When the five feedback loops are closed, there is an additional 10 dB reduction of the flexural response and sound radiation below about 200 Hz. It should be emphasized that both the response and sound radiation at low frequencies was quite high compared to those at higher frequencies. Therefore the five feedback control loops produce a significant effect such that the response and sound radiation in the whole 0 Hz – 1 kHz are brought down to a constant low level.

## 7. Concluding remarks

This paper has presented a comprehensive overview of the principal characteristics of smart panels equipped with feed-forward and feedback multi-channel and single-channel systems for the control of the flexural response and sound transmission due respectively to tonal and to broadband acoustic disturbances. All configurations are composed by a flat aluminum core panel equipped with point/distributed sensors and point/distributed actuators, which encompass arrays of small square/triangular piezoelectric patch actuators, a large piezoelectric foil with quadratically shaded electrodes sensor/actuator, arrays of miniaturized MST accelerometer sensors, arrays of microphone sensors and arrays of proof-mass electromagnetic actuators. The sensor–actuator configurations and the control architectures of all panels considered in the study are suitably displayed in Table 2–5. The principal conclusions drawn from the study on the panels implementing feed-forward systems for the control of tonal disturbances can be summarized in the following points.

- (1) The multi-channel systems with a) the  $4 \times 4$  array of square piezoelectric patch actuators, b) the perimetric 16 triangular piezoelectric actuators, c) the  $3 \times 3$  array of proof-mass electromagnetic actuators, set to minimize the total sound radiation estimated by 5 microphone sensors, generate significant reductions of the flexural response and sound transmission up to a certain cutoff frequency. The control bandwidth depends on both the number of control actuators and the number of microphone error sensors. In general, these systems operate in two ways. Firstly, at low frequencies where the flexural vibration is characterized by the resonant responses of low order flexural modes, they tend to mitigate the resonant response of each mode. Secondly, at higher frequencies where the flexural vibration is characterized by the overlap of the resonant responses of multiple flexural modes, they tend to rearrange, and in some case even to enhance, the response of specific modes in such a way as to obtain a destructive mutual sound radiation effect between the overlapping modes.
- (2) The multi-channel systems with a) the  $4 \times 4$  array of square piezoelectric patch actuators and b) the  $3 \times 3$  array of proof-mass electromagnetic actuators, set to minimize the vibration of the panel measured by arrays of collocated accelerometers, generate limited reductions of the flexural response and sound

transmission. This is because they tend to pin the panel at the error positions such that new flexural modes characterized by 'quilted' shapes are generated, which radiate sound more efficiently.

- (3) The multi-channel system with the 16 perimetric triangular piezoelectric actuators, set to minimize the vibration of the panel measured by 16 accelerometers at their tips, generates quite significant reductions of the sound transmission. This is because the system attenuates the vibration along the perimeter and thus reduces the vibrating surface of the panel such that, overall, there is a lower sound transmission.
- (4) The single-channel systems with a) the  $4 \times 4$  array of square piezoelectric patch actuators and b) the  $3 \times 3$  array of proof-mass electromagnetic actuators, set to minimize the total sound radiation estimated by 5 microphone sensors, produce good reductions of the sound transmission at low frequencies where the sound radiation is controlled by the volumetric vibration of the panel. These systems would not work well if they were set to cancel the volumetric vibration of the panel estimated by arrays of collocated accelerometers since, as discussed in point 2, they would tend to pin the panel and thus increase the sound radiation.
- (5) The single-channel systems formed by a piezoelectric foil with quadratically shaded electrodes effectively reduce the sound transmission both when the actuator is set to minimize the total sound radiation estimated by 5 microphone sensors or to minimize the volumetric vibration of the panel measured with a matched piezoelectric foil with quadratically shaded electrodes. The latter is a rather compact and lightweight solution, which, however, requires a careful design to ensure the coupling between the two transducers occurs via out-of-plane flexural vibrations rather than in-plane extensional and shear vibrations.

The principal conclusions drawn from the study on the panels implementing feedback control systems for the control of broadband disturbances can be summarized in the following points.

- (1) The multi-channel systems, which implement decentralized velocity feedback loops using a) the  $4 \times 4$  array square piezoelectric patch actuators, b) the 16 perimetric triangular piezoelectric patch actuators, c) the  $3 \times 3$  array of proof-mass electromagnetic actuators with collocated accelerometer sensors, generate active damping effects, which effectively dampen the resonant responses of the low order flexural modes of the panel. As a result, both the flexural response and the sound transmission are significantly reduced up to a cutoff frequency, which is determined by the density of feedback loops.
- (2) These decentralized velocity feedback loops require a precise tuning of the control gains since, for large values, the feedback actions tend to pin the panel at the error sensor positions so that no active damping is generated. In this case, the response and sound transmission of the structure is characterized once more by the resonant responses of new lightly damped flexural modes, which are characterized by higher natural frequencies and modified shapes due to the pinning constraints produced by the feedback loops. In particular, the panels with the  $4 \times 4$  array of square



piezoelectric patch actuators and the  $3 \times 3$  array of proof-mass electromagnetic actuators generate the typical 'quilted' mode shapes which radiate sound more effectively such that, overall, the sound transmission is increased rather than reduced.

- (3) The single channel velocity feedback loop based on a) the  $4 \times 4$  array of square piezoelectric patch actuators, b) the  $3 \times 3$  array of proof-mass electromagnetic actuators with at their centers accelerometer sensors, effectively dampen the low order volumetric modes, which are responsible for the sound transmission at low frequencies. Nevertheless, also in this case the feedback gain must be carefully tuned to generate the desired active damping action. Indeed, with large feedback gains, the feedback action tends to pin the panel at the 16 error sensor positions so that no active damping is generated. Accordingly, the flexural response and sound transmission is controlled by the resonant response of new lightly damped modes, which radiate sound more efficiently.
- (4) The single channel velocity feedback loop using a matched volume velocity sensor and uniform force actuator made from piezoelectric foils with quadratically shaded electrodes bonded on either side of the panel effectively controls the low frequency volumetric modes of the panel and thus the low frequency sound transmission through the panel. This distributed sensor-actuator pair doesn't show the pinning effect that characterizes the systems using point sensors. Therefore, the control gain does not need fine tuning. On the contrary, a large gain is sufficient to cancel the error signal, that is to cancel the volumetric vibration component of the panel measured by distributed sensor, which primarily contributes to the sound transmission at low frequencies.

Overall, the study has shown that, multi-channel systems with arrays of small sensors and small actuators can generate significant reductions of the flexural response and noise transmission over a wide low audio frequencies band. For feed-forward control, the multi-channel systems should rely on microphone sensors, which estimate the radiated sound field. Alternatively, for feedback control, the decentralized multi-channel systems should encompass collocated and dual structural sensor-actuator pairs. However, both architectures may be affected by high-frequencies control spillover, which could arise respectively from the coarse estimate of the sound radiation with a finite number of microphones or the so called 'pinning effect' generated at the structural error sensors. These drawbacks can be suitably overcome by single-channel feed-forward and feedback systems using collocated and dual distributed piezoelectric sensor-actuator pairs, which cover the whole surface of the panel. For instance, the electrodes of the piezoelectric transducers can be conveniently shaded in such a way as the sensor measures the volumetric vibration of the panel and the actuator excites the volumetric vibration of the panel. In this case, either control architectures can be set to minimize, with limited control spillover effects, the volumetric vibration of the panel. In this way, the flexural response and noise transmission can be effectively reduced, although, compared to multi-channel systems, over a smaller low audio frequencies band.

## Acknowledgments

The authors would like to acknowledge the support provided by the DEVISU project which was funded by the Ministero dell'Istruzione, dell'Università e della Ricerca research funding programme PRIN 2017 [2017ZX9X4K].

## Disclosure statement

No potential conflict of interest was reported by the authors.

## Funding

This work was supported by DEVISU project which was funded by the Ministero dell'Istruzione, dell'Università e della Ricerca, research funding programme PRIN 2017 [2017ZX9X4K].

## References

- [1] Thompson DJ, Dixon J. Vehicle Noise, In: Fahy FJ, Walker JG, editors. *Advanced Applications in Acoustics, Noise and Vibration*. London: Spon Press; 2004. p. 236–291.
- [2] Thompson DJ. *Railway Noise and Vibration: mechanisms, Modelling and Means of Control*. Amsterdam: Elsevier; 2009.
- [3] Mixson JS, Wilby JS. *Interior Noise*, in *Aeroacoustics of Flight Vehicles, Theory and Practice*. Hubbard HH, ed.. Hampton: NASA Reference Publications; 1995. p. 271–356.
- [4] Wang X. *Vehicle noise and vibration refinement*. New York: CRC Press; 2010.
- [5] Reddy JN. *Mechanics of Laminated Composite Plates, Theory and Analysis*. London: CRC Press; 1997.
- [6] Fahy F, Gardonio P. *Sound and Structural Vibration*, 2nd ed.. London: Academic Press; 2007.
- [7] Zardian MG, Moslemi N, Mozafari F, et al. Flexural and free vibration control of smart epoxy composite beams using shape memory alloy wires actuator. *J Intell Mater Syst Struct*. 2020;31(13):1557–1566.
- [8] Claeys C, Deckers E, Pluymers B, et al. A lightweight vibro-acoustic metamaterial demonstrator: numerical and experimental investigation. *Mech Syst Signal Pr*. 2016;70-71:853–880.
- [9] de Melo Filho NGR, Claeys C, Deckers E, et al. Metamaterial foam core sandwich panel designed to attenuate the mass-spring-mass resonance sound transmission loss dip. *Mech Syst Signal Pr*. 2020;139:106624.
- [10] Brennan MJ, Ferguson NS. *Vibration control*, in *Advanced Applications in Acoustics, Noise and Vibration*. Fahy FJ, Walker JG, eds.. London: Spon Press; 2004. p. 530–580.
- [11] Thompson D. *Noise Control*, in *Fundamentals of Sound and Vibration*. Fahy F, Thompson D, eds.. Chichester, UK: CRC Press; 2015. p. 213–310.
- [12] Sagartzazu X, Hervella-Nieto L, Pagalday JM. Review in sound absorbing materials. *Arch Comput Methods Eng*. 2008;15: 311–342.
- [13] Arenas JP, Crocker MJ. Recent trends in porous sound-absorbing materials. *J Sound Vib*. 2010;44:12–17.
- [14] Sun JQ, Jolly MR, Norris MA. Passive, adaptive and active tuned vibration absorbers—a survey. *J Vib Acoustics*. 1995;117: 234–242.
- [15] Brennan MJ. Vibration control using a tunable vibration neutralizer. *Proc Inst Mech Eng C J Mech Eng Sci*. 1997;211: 91–108.
- [16] Turco E, Gardonio P. Sweeping shunted electro-magnetic tuneable vibration absorber: design and implementation. *J Sound Vib*. 2017;407:82–105.
- [17] Turco E, Gardonio P, Petrella R, et al. Modular vibration control unit formed by an electro-magnetic proof-mass transducer and sweeping resistive-inductive shunt. *J Vib Acoust*. 2020;142:1–16. [0610005].

- [18] Gardonio P, Casagrande D. Shunted piezoelectric patch vibration absorber on two-dimensional thin structures: tuning considerations. *J Sound Vib.* **2017**;395:26–47.
- [19] Casagrande D, Gardonio P, Zilletti M. Smart panel with time-varying shunted piezoelectric patch absorbers for broadband vibration control. *J Sound Vib.* **2017**;400:288–304.
- [20] Dal Bo L, Gardonio P, Casagrande DE, et al. Smart panel with sweeping and switching piezoelectric patch vibration absorbers: experimental results. *Mech Syst Signal Pr.* **2019**;120:308–325.
- [21] Fuller CR, Elliott SJ, Nelson PA. *Active Control of Vibration.* London: Academic Press; **1996.**
- [22] Nelson PA, Elliott SJ. *Active Control of Sound.* London: Academic Press; **1992.**
- [23] Gardonio P, Turco E. Tuning of vibration absorbers and Helmholtz resonators based on modal density/overlap parameters of distributed mechanical and acoustic systems. *J Sound Vib.* **2019**;451:32–70.
- [24] Gardonio P. Active Noise Control. In: Blockley R, Shyy W, editors. *Encyclopedia of Aerospace Engineering.* Chichester, UK: John Wiley & Sons Ltd; **2010.** p. 3575–3588.
- [25] Elliott SJ. *Signal Processing for Active Control.* London: Academic Press; **2000.**
- [26] Rohlfing J, Gardonio P. Homogeneous and sandwich active panels under deterministic and stochastic excitation. *J Acoust Soc Am.* **2009**;125:3696–3706.
- [27] Gardonio P, Lee YS, Elliott SJ, et al. Analysis and measure of a matched volume velocity sensor and uniform force actuator for active structural acoustic control. *J Acoust Soc Am.* **2001**;110:3025–3031.
- [28] Gardonio P, Elliott SJ. Smart panels for active structural acoustic control. *Smart Mater Struct.* **2004**;13:1314–1336.
- [29] Gardonio P, Elliott SJ. Smart panels with velocity feedback control systems using triangularly shaped strain actuators. *J Acoust Soc Am.* **2005**;117:2046–2064.
- [30] Gonzalez Diaz C, Gardonio P. Feedback control laws for proof-mass electro-dynamic actuators. *Smart Mater Struct.* **2007**;16:1766–1783.
- [31] Gardonio P. *Composite Smart Panels for Active Control of Sound Radiation*, in *Encyclopedia of Composites*, 2nd ed.. Nicolais L, Borzacchiello A, eds.. Hoboken, New Jersey: John Wiley & Sons; **2012.** p. 558–579.
- [32] Gardonio P. Boundary Layer Noise – part 2: interior Noise Radiation and Control. In: Camussi R, editor. *Noise Sources In Turbulent Shear Flows: fundamentals And Applications.* Udine: Springer; **2013.** p. 379–448.
- [33] Bianchi E, Gardonio P, Elliott SJ. Smart panel with multiple decentralised units for the control of sound transmission. Part III: control system implementation. *J Sound Vib.* **2004**;274:215–232.
- [34] Gonzalez Diaz C, Paulitsch C, Gardonio P. Smart panel with active damping units. Implementation of decentralized control. *J Acoust Soc Am.* **2008**;124:898–910.
- [35] Gardonio P, Aoki Y, Elliott SJ. A smart panel with active damping wedges along the perimeter. *Smart Mater Struct.* **2010**;19:1–15.
- [36] Paulitsch C, Gardonio P, Elliott SJ, et al. *Design of a lightweight, electrodynamic, inertial actuator with integrated velocity sensor for active vibration control of a thin lightly-damped panel*, Proceedings of the International Conference on Noise and Vibration Engineering (ISMA), Katholieke Universiteit Leuven, Belgium, 20–23 September **2004.** pp 239–254.
- [37] Gonzalez Diaz C, Paulitsch C, Gardonio P. Active damping control unit using a small scale proof mass electrodynamic actuator. *J Acoust Soc Am.* **2008**;124:886–897.
- [38] Clark RL, Saunders WR, Gibbs GP. *Adaptive Structures.* New York: John Wiley & Sons Inc; **1998.**
- [39] Preumont A. *Vibration control of Active Structures.* 4th ed. Berlin: Springer; **2018.**
- [40] Elliott SJ, Gardonio P, Sors TJ, et al. Active vibroacoustic control with multiple local feedback loops. *J Acoust Soc Am.* **2002**;111:908–915.
- [41] Petitjean B, Legrain I. Feedback controllers for active vibration suppression. *J Struct Control.* **1996**;3: 111–127.

- [42] Petitjean B, Legrain I, Simon F, et al. Active control experiments for acoustic radiation reduction of a sandwich panel: feedback and feedforward investigations. *J Sound Vib.* 2002;252:19–36.
- [43] Gardonio P, Miani S, Blanchini F, et al. Plate with decentralised velocity feedback loops: power absorption and kinetic energy considerations. *J Sound Vib.* 2012;331:1722–1741.
- [44] Gardonio P, Bianchi E, Elliott SJ. Smart panel with multiple decentralised units for the control of sound transmission. Part II: design of the decentralised control units. *J Sound Vib.* 2004;274:193–213.
- [45] Rohlffing J, Gardonio P, Thompson DJ. Comparison of decentralized velocity feedback control for thin homogeneous and stiff sandwich panels using electrodynamic proof-mass actuators. *J Sound Vib.* 2011;330:843–867.
- [46] Maciejowski JM. *Multivariable Feedback Design*. New York: Addison-Wesley; 1989 [1989].
- [47] Skogestad S, Postlethwaite I. *Multivariable Feedback Control*. New York: John Wiley and Sons; 1996.
- [48] Aoki Y, Gardonio P, Gavagni M, et al. Parametric study of a piezoceramic patch actuator for proportional velocity feedback control loop. *J Vib Acoust.* 2010;132:1–10. [061007].
- [49] Matunaga S, Yu Y, Ohkami Y. Vibration suppression using acceleration feedback control with multiple proof-mass actuators. *AIAA J.* 1997;35:856–862.
- [50] Benassi L, Elliott SJ. Active vibration isolation using an inertial actuator with local displacement feedback control. *J Sound Vib.* 2004;278:705–724.
- [51] Benassi L, Elliott SJ, Gardonio P. Active vibration isolation using an inertial actuator with local force feedback control. *J Sound Vib.* 2004;276:157–179.
- [52] Paulitsch CP, Gardonio P, Elliott SJ. Active vibration control using an inertial actuator with variable internal damping. *J Acoust Soc Am.* 2006;119:2131–2140.
- [53] Rohlffing J, Gardonio P, Elliott SJ. Feedback compensator for control units with proof-mass electrodynamic actuators. *J Sound Vib.* 2012;331:3437–3450.
- [54] Dal Borgo M, Tehrani MG, Elliott SJ. *Nonlinear control and stability analysis of a stroke limited inertial actuator in velocity feedback*. Proceedings of the 9th European Nonlinear Dynamics Conference ENOC, 2(4) (2017) 1–10.
- [55] Lindner DK, Zvonar GA, Borojevic D. Nonlinear control of a proof mass actuator. *J Guid Control Dyn.* 1997;20: 464–470.
- [56] Kras A, Gardonio P. Velocity feedback control with a flywheel proof mass actuator. *J Sound Vib.* 2017;402:31–50.
- [57] Kras A, Gardonio P. Active vibration control unit with a flywheel inertial actuator. *J Sound Vib.* 2020;464:1–20.
- [58] Johnson ME, Elliott SJ. Active control of sound radiation using volume velocity cancellation. *J Acoust Soc Am.* 1995;98:2174–2186.
- [59] Clark RL, Fuller CR. Experiments on active control of structurally radiated sound using multiple piezoceramic actuators. *J Acoust Soc Am.* 1992;91:3313–3320.
- [60] Fuller CR. Active control of sound transmission/radiation from elastic plates by vibration inputs: I—analysis. *J Sound Vib.* 1990;136:1–15.
- [61] Fuller CR, Hansen CH, Snyder SD. Active control of sound radiation from a vibrating rectangular panel by sound sources and vibration inputs: an experimental comparison. *J Sound Vib.* 1991;145:195–215.
- [62] Burdisso RA, Fuller CR. Dynamic behaviour of structures in feedforward control of sound radiation. *J Acoust Soc Am.* 1992;92:277–286.
- [63] Baumann WT, Ho F-S, Robertshaw HH. Active structural acoustic control of broadband disturbances. *J Acoust Soc Am.* 1992;92:1998–2005.
- [64] Clark RL, Fuller CR. A model reference approach for implementing active structural acoustic control. *J Acoust Soc Am.* 1992;92:1534–1544.
- [65] Fuller CR, Rogers CA, Robertshaw HH. Control of sound radiation with active/adaptive structures. *J Sound Vib.* 1992;145:19–39.
- [66] Fuller CR, Burdisso RA. A wavenumber domain approach to the active control of structure-borne sound. *J Sound Vib.* 1992;148:355–360.

- [67] Clark RL, Fuller CR. Active structural acoustic control with adaptive structures including wavenumber considerations. *J Int Mat Syst Struct.* 1992;3: 296–315.
- [68] Elliott SJ, Johnson ME. Radiation modes and the active control of sound power. *J Acoust Soc Am.* 1993;94:2194–2204.
- [69] Snyder SD, Tanaka N, Kikushima Y. The use of optimally shaped piezoceramic–electric film sensors in the active control of free field structural radiation. Part 1: feedforward control. *J Vib Acoust.* 1996;117:311–322.
- [70] Fuller CR, Silcox RJ. Active structural acoustic control. *J Acoust Soc Am.* 1992;91:519.
- [71] Li WL, Gibeling HJ. Determination of the mutual radiation resistances of a rectangular plate and their impact on the radiated sound power. *J Sound Vib.* 2000;229:1213–1233.
- [72] Li WL. An analytical solution for the self- and mutual radiation resistances of a rectangular plate. *J Sound Vib.* 2001;245:1–16.
- [73] Henriouille K, *Distributed actuators and sensors for active noise control*, PhD thesis, Katholieke Universiteit Leuven, 2001.
- [74] Burke SE, Hubbard JE Jr. Distributed transducer vibration control of thin plates. *J Acoust Soc Am.* 1991;90:937–944.
- [75] Maillard JP, Fuller CR. Advanced time domain wave-number sensing for structural acoustic systems. I. Theory and design. *J Acoust Soc Am.* 1994;95:3252–3261.
- [76] Masson P, Berry A, Nicolas J. Active structural acoustic control using strain sensing. *J Acoust Soc Am.* 1997;102:1588–1599.
- [77] Maillard JP, Fuller CR. Comparison of two structural sensing approaches for active structural acoustic control. *J Acoust Soc Am.* 1998;103:396–400.
- [78] Gibbs GP, Clark RL, Cox DE, et al. Radiation modal expansion: application to active structural acoustic control. *J Acoust Soc Am.* 2000;107:332–339.
- [79] Preumont A, Francois A, Durbru S. Piezoceramic array sensing for real-time, broad-band sound radiation measurement. *J Vib Acoust.* 1999;121:446–452.
- [80] Francois A, De Man P, Preumont A. Piezoceramic array sensing of volume displacement: a hardware demonstration. *J Sound Vib.* 2001;244:395–405.
- [81] Lee Y-S, Gardonio P, Elliott SJ. Volume velocity vibration control of a smart panel using a uniform force actuator and an accelerometer array. *Smart Mater Struct.* 2002;11:863–873.
- [82] Dimitriadis EK, Fuller CR, Rogers CA. Piezoceramic actuators for distributed vibration excitation of thin plates. *J Vib Acoust.* 1991;113:100–107.
- [83] Rogers CA, Liang C, Fuller CR. Modelling of shape memory alloy hybrid composites for structural acoustic control. *J Acoust Soc Am.* 1991;89:210–220.
- [84] Clark RL, Fuller CR, Wicks AL. Characterization of multiple piezoceramic actuators for structural excitation. *J Acoust Soc Am.* 1991;90:346–357.
- [85] Clark RL, Fleming MR, Fuller CR. Piezoceramic actuators for distributed vibration excitation of thin plates. *J Vib Acoust.* 1993;115:332–339.
- [86] Zhou SW, Liang C, Rogers CA. Modelling of distributed piezoceramic actuators integrated with thin cylindrical shells. *J Acoust Soc Am.* 1994;96:1605–1612.
- [87] Sullivan JM, Hubbard JE Jr., Burke SE. Modelling approach for two-dimensional distributed transducers of arbitrary spatial distribution. *J Acoust Soc Am.* 1996;99:2965–2974.
- [88] Sullivan JM, Hubbard JE Jr., Burke SE. Distributed sensor/actuator design for plates: spatial shape and shading as design parameters. *J Sound Vib.* 1997;203:473–493.
- [89] Sutton TJ, Johnson ME, Elliott SJ, *A distributed actuator for the active control of sound transmission through a partition*. Proc. of the 6th International Conference on Recent Advances on Structural Dynamics, Southampton, United Kingdom, 1997, 1247–1255.
- [90] Clark RL, Fuller CR. Optimal placement of piezoceramic actuators and polyvinylidene fluoride error sensors in active structural acoustic control approaches. *J Acoust Soc Am.* 1992;92:1521–1533.
- [91] Borgiotti GV. The power radiated by a vibrating body in an acoustic fluid and its determination from boundary measurements. *J Acoust Soc Am.* 1990;88:1884–1893.
- [92] Baumann WT, Saunders WR, Robertshaw HH. Active suppression of acoustic radiation from impulsively excited structures. *J Acoust Soc Am.* 1991;88:3202–3208.

- [93] Naghshineh K, Koopmann GH, Belegundu AD. Material tailoring of structures to achieve a minimum radiation condition. *J Acoust Soc Am*. 1992;92:841–855.
- [94] Naghshineh K, Koopmann GH. Active control of sound power using acoustic basis functions as surface velocity filters. *J Acoust Soc Am*. 1993;93:2740–2752.
- [95] Cunefare KA. The minimum multimodal radiation efficiency of baffled finite beams. *J Acoust Soc Am*. 1991;90:2521–2529.
- [96] Gardonio P, Brennan MJ. Mobility and impedance methods in structural dynamics. In: Fahy FJ, Walker J, editors. *Advanced applications in acoustics, noise and vibration*. London: Spon Press; 2004. p. 389–447.
- [97] Wang B-T, Fuller CR, Dimitriadis EK. Active control of noise transmission through rectangular plates using multiple piezoceramic or point force actuators. *J Acoust Soc Am*. 1991;90:2820–2830.
- [98] Thompson D, Gardonio P, Rohlfling J. Can a transmission coefficient be greater than unity? *Appl Acousti*. 2009;70: 681–688.
- [99] Maury C, Gardonio P, Elliott SJ. Active control of the flow-induced noise transmitted through a panel. *AIAA J*. 2001;39:1860–1867.
- [100] Maury C, Gardonio P, Elliott SJ. Model for active control of flow-induced noise transmitted through a double partitions. *Aiaa J*. 2002;40:1113–1121.
- [101] Thomas DR, Nelson PA. Feedback control of sound radiation from a plate excited by a turbulent boundary layer. *J Acoust Soc Am*. 1995;98:2651–2662.
- [102] Clark RL, Cox DE. Multi-variable structural acoustic control with static compensation. *J Acoust Soc Am*. 1996;102:2747–2756.
- [103] Dehandschutter W, Henriouille K, Swevers J, et al. Feedback control of broadband sound radiation using a volume velocity sensor. *Proc. of ACTIVE 97*. Budapest, Hungary, 1997;979–992.
- [104] Cox DE, Gibbs GP, Clark RL, et al. Experimental robust control of structural acoustic radiation. *J Vib Acoust*. 1999;121:433–439.
- [105] Viperman JS, Clark RL. Acoustic power suppression of a panel structure using  $H_\infty$  output feedback control. *J Acoust Soc Am*. 1999;105:219–225.
- [106] Seto K, Ren M, Doi F. Modelling and feedback structural acoustic control of a flexible plate. *J Vib Acoust*. 2001;123:18–23.
- [107] Smith GC, Clark RL. A crude method of loop-shaping adaptive structures through optimum spatial compensator design. *J Sound Vib*. 2001;247:489–508.
- [108] Henry JK, Clark RL. Active control of sound transmission through a curved panel into a cylindrical enclosure. *J Sound Vib*. 2002;249:325–349.
- [109] Chang W, Varadan SV, Varadan VK. Design of robust vibration controller for a smart panel using finite element model. *J Vib Acoust*. 2002;124:265–276.
- [110] Doyle JC, Glover K, Khargonekar PP, et al. State-space solutions to standard  $H_2$  and  $H_\infty$  control problems. *IEEE Trans Autom Control*. 1989;34:831–847.
- [111] Boyd S, Barratt C. *Linear Controller Design: limits of Performance*. Englewood Cliffs, NJ: Prentice-Hall; 1991.
- [112] Frampton KD, Bauman ON, Gardonio P. A comparison of decentralized, distributed, and centralized vibro-acoustic control. *J Acoust Soc Am*. 2010;128(5):2798–2806.
- [113] Snyder SD, Tanaka N, Kikushima Y. The use of optimally shaped piezoceramic-electric film sensors in the active control of free field structural radiation. Part 2: feedback control. *J Vib Acoust*. 1996;118:112–121.
- [114] De Man P, Francois A, Preumont A. Robust feedback control of a baffled plate via open-loop optimization. *J Vib Acoust*. 2002;124:154–157.
- [115] Bingham B, Atalla MJ, Hagood NW. Comparison of structural-acoustic control designs on an active composite panel. *J Sound Vib*. 2001;244:761–778.
- [116] Heatwole CH, Franchek MA, Bernhard RJ. Robust feedback control of flow-induced structural radiation of sound. *J Acoust Soc Am*. 1997;102:989–997.

- [117] Burke SE, Hubbard JE Jr, Meyer JE. Distributed transducers and collocation. *Mech Syst Signal Pr.* 1993;7:765–770.
- [118] Sun JQ. Some observations on physical duality and collocation of structural control sensors and actuators. *J Sound Vib.* 1996;194:765–770.
- [119] Jayachandran V, Sun JQ. Unconditional stability domains of structural control systems using dual actuator-sensor pairs. *J Sound Vib.* 1997;208:159–166.
- [120] Balas MJ. Direct velocity control of large space structures. *J Guidance Control.* 1979;2:252–253.
- [121] Joshi SM. *Control of Large Flexible Space Structures.* London: Springer; 1989.
- [122] Ahmadian M, Guilio AP. *Recent advances in the use of piezoceramics for vibration suppression, shock vib. Dig.* 2001;33:15–22.
- [123] Sessler GM. Piezoelectricity in polyvinylidene fluoride. *J Acoust Soc Am.* 1981;70:1596–1608.
- [124] Reddy JN. *Theory and Analysis of Elastic Plates and Shells.* Boca Raton: CRC Press; 2006.
- [125] Reddy JN. *Energy and Variational Methods in Applied Mechanics.* New York: Wiley & Sons; 1984.
- [126] Banks HT, Smith RC, Wang Y. *Smart Material Structures, Modeling, Estimation and Control.* Chichester: Wiley & Sons; 1996.
- [127] Preumont A. *Mechatronics, Dynamics of Electromechanical and Piezoelectric Systems.* Dordrecht: Springer; 2006.
- [128] Lee CK. Theory of laminated piezoceramic plates for the design of distributed sensor/actuators. Part I: governing equations and reciprocal relationships. *J Acoust Soc Am.* 1990;87:1144–1158.
- [129] Deraemaeker A, Tondreau G, Bourgeois F. Equivalent loads for two-dimensional distributed anisotropic piezoelectric transducers with arbitrary shaped attached to thin plate structures. *J Acoust Soc Am.* 2011;129:681–690.
- [130] van der Ziel A. *Solid state physical electronics.* London: Prentice-Hall; 1968.
- [131] Lee CK, Moon FC. Laminated piezopolymer plates for torsion and bending sensors and actuators. *J Acoust Soc Am.* 1989;85:2432–2439.
- [132] Lee CK, Moon FC. Modal sensors/actuators. *J Appl Mech.* 1990;57:434–441.
- [133] Lee CK, Chiang WW, O'Sullivan TC. Piezoelectric modal sensor/actuator pairs for critical active damping vibration control. *J Acoust Soc Am.* 1991;90:374–384.
- [134] Sonti V, Kim S, Jones J. Equivalent forces and wavenumber spectra of shaped piezoelectric actuators. *J Sound Vib.* 1995;187:111–131.
- [135] Preumont A, Francois A, De Man P, et al. Spatial filters in structural control. *J Sound Vib.* 2003;265:61–79.
- [136] Gohari S, Sharifi S, Vrcelj Z. New explicit solution for static shape control of smart laminated cantilever piezo-composite-hybrid plates/beams under thermo-electro-mechanical loads using piezoelectric actuators. *Compos Struct.* 2016;145:89–112.
- [137] Gohari S, Sharifi S, Vrcelj Z. A novel explicit solution for twisting control of smart laminated cantilever composite plates/beams using inclined piezoelectric actuators. *Compos Struct.* 2017;161:477–504.
- [138] Soheil G, Shokrollah S, Rouzbeh A, et al. A quadratic piezoelectric multi-layer shell element for FE analysis of smart laminated composite plates induced by MFC actuators. *Smart Mater Struct.* 2018;27(9).
- [139] Lee Y-S, Gardonio P, Elliott SJ. Coupling analysis of a matched piezoelectric sensor and actuator pair for vibration control of a smart beam. *J Acoust Soc Am.* 2002;111:2715–2726.
- [140] Gardonio P, Elliott SJ. Modal response of a beam with a sensor–actuator pair for the implementation of velocity feedback control. *J Sound Vib.* 2005;284:1–22.